Natural Resources Canada | Ressources naturelles Canada

GEOLOGICAL SURVEY OF CANADA
OPEN FILE 7621

Ocean Bottom Seismometer Experiment on the Beaufort shelf and slope region conducted during Expedition ARA04C on the IBRV Araon

M. Riedel, M. Ulmi, K.W. Conway, G. Standen, A. Rosenberger, J.K. Hong, Y.K. Jin, H.S. Kim, S.R. Dallimore

2014

Canada

GEOLOGICAL SURVEY OF CANADA
OPEN FILE 7621

Ocean Bottom Seismometer Experiment on the Beaufort shelf and slope region conducted during Expedition ARA04C on the IBRV Araon

M. Riedel[1], M. Ulmi[1], K.W., Conway[1], G. Standen[2], A. Rosenberger[3], J.K. Hong[4], Y.K. Jin[4], H.S. Kim[5], S.R. Dallimore

[1] Natural Resources Canada, Geological Survey of Canada, 9860 West Saanich Road, Sidney, British Columbia
[2] Geoforce Consultants Ltd., 1 Endeavour Drive, Argo Building, Bedford Institute of Oceanography, Dartmouth, Nova Scotia
[3] Arescon Research Ltd., Sidney, British Columbia
[4] Korea Polar Research Institute (KOPRI), 26 Songdomirae-ro, Yeonsu-gu Incheon, 406-840, Korea
[5] Korea Gas Corporation, 5th Floor, Korea Paperless Trade Centre, 688 Sampyeong-dong, Bundang-gu, Seongnam-si, Gyeinggi, Korea

2014

doi:10.4095/295550

This publication is available for free download through GEOSCAN (http://geoscan.nrcan.gc.ca/).

Recommended citation
Riedel, M., Ulmi, M., Conway, K.W., Standen, G., Rosenberger, A., Hong, J.K., Jin, Y.K., Kim, H.S., and Dallimore, S.R., 2014. Ocean Bottom Seismometer Experiment on the Beaufort shelf and slope region conducted during Expedition ARA04C on the IBRV Araon; Geological Survey of Canada, Open File 7621, 55p. doi:10.4095/295550

Publications in this series have not been edited; they are released as submitted by the author.

Abstract

Expedition ARA04C (conducted from September 10 – September 26, 2013 in Canadian waters) on the Korean icebreaker IBRV Araon was laid out to investigate the Beaufort Sea shelf and slope region and collect geo-scientific data for various aspects relevant to the GSC's mandated regional geo-hazard assessment of the offshore Beaufort region. A critical element of the geo-hazards is the distribution of permafrost across the submerged shelf. To address this question a set of six Ocean Bottom Seismometers (OBS) were deployed in a grid pattern across the near shelf-edge zone, and a set of three OBS was used in a second deployment along a central shelf-crossing north-east to south-west oriented line. Initial data processing was carried out, which is required for any follow-up detailed velocity analysis. The processing included definition of exact shot times, geometry calculation, OBS position re-location, and OBS orientation analysis. A preliminary analysis of the hydrophone and vertical-component data from the OBS stations reveals a P-wave-velocity structure with values ranging from 1800 m/s to over 4000 m/s indicative of wide-spread ice-bearing sediments. This open-file report also contains the digital OBS data for all stations in standard SEGY format, together with the required raw and processed geometry information.

1 Introduction

A two-ship scientific research expedition in the southern Beaufort Sea was carried out between September 10 to October 10, 2013, using the research icebreaker Araon operated by the Korea Polar Research Institute (KOPRI) and the Canadian Coast Guard Ship (CCGS) Sir Wilfrid Laurier. The multidisciplinary science program included geological, geophysical, and oceanographic investigations of the continental shelf and slope. The research conducted will help improve the understanding of geohazards in this setting by assessing the regional geology, the stability of decomposing offshore permafrost and gas hydrates, mechanisms for surficial gas/fluid migration, and active geologic processes. Priorities for the Araon Expedition ARA04C (see Figure 1 for a complete ship track) included a multi-channel seismic (MCS) survey in combination with Ocean Bottom Seismometers (OBS) with the goal to collect site-survey data supporting the Integrated Ocean Drilling Program (IODP) pre-proposals 806 (Dallimore et al., 2012) and 753 (O'Regan, et al. 2010). The combination of the MCS survey with OBS instruments offers a unique opportunity to study permafrost settings. To enhance our understanding of the presence (or absence) of permafrost in the subsurface is a key objective of this expedition, and is a cornerstone of the IODP pre-proposal 806. Predictions of the offshore permafrost distribution were made in the past using several techniques including borehole temperature data (see e.g. Hu et al., 2013) and refraction seismic studies (Pullan et al., 1987). The offshore-edge of the permafrost in ~100 m water depth is the most critical boundary for understanding the sediment and hydro-geologic regimes associated with the degrading permafrost. Following the strategy of collecting data along main shelf-edge perpendicular transects as outlined in Figure 2, we deployed nine OBS along three transects bracketing the area of apparent continuous permafrost with ice-bonded sediments to the South-East and the ice-free, no permafrost zone at the North-West end of the transects (Figure 3). Two areas of across-shelf transects were chosen: Area 1, focusing on the "yellow" priority transect, and Area 2, focusing on the "red" priority transect.

Sea ice conditions were challenging throughout the entire expedition and mandated a deployment scheme that would allow collecting airgun data for the OBS seismic reflection and refraction experiment and having an opportunity of OBS retrieval in relatively ice-free waters. Due to extended ice along the "red" priority transect at the beginning of Expedition ARA04C, we first started operation along the "yellow" transect area and only attempted to work along the

"red" priority transect later in the program, when ice had moved farther to the North. However, although ice conditions were more favorable when operating along the "red" priority transect, the program was interrupted by a storm with winds over 40 knots and seas of up to 5 meter.

This report details the technical specifications of the OBS, outlines the geometry definition, and explains the steps of the OBS relocation analysis, which is required prior to any velocity analysis. We also highlight one approach to define the orientation of the OBS geophones relative to true North and define a tilt-estimate for the vertical geophone component. The geophone orientation is important for any wave-field separation processing and shear-wave analysis.

2 Ocean Bottom Seismometer technical details and data collected

The NRCan owned digital OBS are instruments which are designed to collect seismic data while lying on the ocean floor. Each unit has a packaged array of three geophones (one vertical, two horizontal) and a single hydrophone, which measure both passive and active-source seismic events (Figure 4). The OBS units consist of one large and two smaller Benthos spheres mounted to a frame. This frame has half-moon shaped cut-outs on either side where the OBS cylinder is fastened using bottom support brackets cut to the same design. The whole unit is then placed on an anchor plate and fastened using the release rod to secure the OBS to the plate. The geophones are fastened to the frame using galvanic release pins. This allows the geophones to release when the unit is sitting on the ocean floor so that they do not become tangled when the unit is descending (Figure 4). A trailing rope is used to recover the unit and brought on board for data downloading and mechanical and electrical checks. Deployment was achieved using the vessel’s A-frame and a simple slip-hook, releasing the OBS into the water as soon as it hits the water level.

The OBS electronics are housed in a full ocean depth pressure housing, which contains the batteries that provide the voltage for running the digital acquisition and analog boards. These boards are designed by Ohmnitech of Dartmouth, Nova Scotia, Canada. The data are written and stored on a 16 Gigabyte flash card, which is removed upon retrieval for data processing. The OBS data are collected on the flash card independently of the operation onboard the vessel. The

individual airgun shots are triggered onboard the ship using the ship's Global Positing System (GPS) antenna and time settings. The computer on the OBS, however, will have some clock drift relative to the vessel's time, which needs to be corrected upon OBS-recovery. Also, the exact time of each airgun shot needs to be recorded to sub-millisecond accuracy to allow for clock-drift corrections and exact shot-point location calculations. Therefore, two separate GPS antennae were mounted on the 2nd deck (helicopter-deck level) on the starboard side connected by cable to two individual time-servers in the dry lab. The OBS time server is connected to the recovered OBS and clock-drift is being calculated (Table 2). This drift will be included in the processing of the OBS data onshore. The second time server is matching incoming trigger data with the exact time and navigation data from the GPS antenna, which will be used to define relative shot locations. The pre-processing of OBS data will then define absolute distances (offsets) from OBS to airgun shots using an OBS-relocation inversion algorithm developed by Prof. Dr. Keith Louden at Dalhousie University, Halifax, Nova Scotia, Canada (see below for more details).

The OBS are programmed to start logging at a given time after deployment and also have a back-up time for auto-release, if the forced acoustic release attempts fail. Once the airgun program is completed, a coded acoustic release command is sent to the individual OBS. A low voltage, high current circuit is used to short out the seawater/ground Minell wire, which then releases the rod holding the anchor and OBS together. After an eight minute burn, the unit then rises at approximately 1 m/s to the surface. Once the unit is at the surface a flashing strobe and a radio direction finder is used to locate the OBS float assembly.

The OBS experiment was split into two separate deployment periods. The first set of six OBS was deployed in the night of September 13 to 14, 2013 (Table 1) at the start of the airgun and MCS program and focused on two lines across the shelf and shelf edge zone of the Transect 1 Area (“yellow” transect, Figure 3). All six OBS were recovered successfully and onboard data quality check confirmed that all OBS recorded data on all four channels (Figure 5). Due to ice over the intended route (Figure 6), two lines crossing the OBS-A (station ARA04C_13OBS_001) had to be shortened at the northern limit, resulting in no direct coverage of OBS-A.

The second deployment was carried out focusing on the Transect 2 Area over the "red" priority transect (Figure 3) after this portion of the study zone became more ice-free and allowed

a complete line covering the shelf and shelf-edge zone and a small mud volcano feature in the slope region (~250 m water depth). The OBS were deployed in the night of September 18, 2013 (Table 1). Two attempts in collecting airgun seismic data along this OBS transect were made: a first attempt started at 17:00 on September 18 along the south-eastern end of the transect with two airgun ramp-up procedures, but no sustainable pressures for continuous airgun operations were reached, and the operation was halted. The ship maintained a route along the intended seismic line towards the north-west as the gear could not be recovered during night. After a short airgun repair operation, a second attempt was started to collect seismic data in the afternoon of September 20, 2013. After only three hours of operation, airgun leakage problems started and the line was finally abandoned by 19:00 on September 20 at about OBS-D (Station ARA04C_29OBS_001). Only OBS-D and OBS-P were recovered during the evening of September 21, 2013. A release attempt on OBS-L was made but no OBS was seen on the surface. After one hour of continued release-code sending, we temporarily abandoned this station. Upon return (OBS-P was recovered in the meantime) a strobe light was spotted on the surface at about 2 nautical miles to the South-East of the OBS-L station, but an additional hour search-loop did not yield any further sightings of the OBS. It is speculated that the OBS did release upon the first attempt, but we were initially too far away from the OBS surfacing point to see it in the twilight and the strobe may not have activated then. Batteries may also not last as long as expected in the cold surface water temperatures in this region and thus we were unable to spot the strobe light during the search-loop later in the evening.

3 Geometry definition and SEGY-Data generation

As described in the previous section, two time-servers were used during the seismic experiment to define absolute time references for the OBS clock drift and airgun shot times. A separate BNC cable was laid from the airgun control unit in the main dry lab of the Araon to a second dry lab where a shot-logger computer was installed together with the time servers. The shot logger computer writes the received trigger signal together with a time-stamp and GPS-antenna navigation location to a hard-disk. The shot-time logger data were regularly copied for backup during the survey. A first step in the geometry calculation for the OBS is the correction of the GPS-antenna position to the actual airgun position (see Figure 7). The GPS antenna for the

shot-logger system was mounted 33m off the stern of the vessel. The geometry of the survey, which includes initial offset calculation between the OBS and airgun array, was done using the Shot-Tab software provided through Prof. Dr. Keith Louden at Dalhousie University, Halifax, Nova Scotia, Canada (Figure 8). Clock-drift information as defined from Table 2 is inserted together with an overall clock-drift that was determined iteratively by trial and error. The software DobstoSgy.exe developed by Prof. Dr. Keith Louden at Dalhousie University is then used to convert the raw OBS data to a SEGY standard. This software allows the user to specify the output lengths of the individual traces (e.g. 10 seconds) and the critical SEGY trace-header information is populated for basic seismic processing and velocity analysis. However, after an initial geometry definition and data conversion to SEGY it was noted that each OBS appears to have an additional constant time offset. This was noted, because the first direct arrival time measured on the nearest trace to the OBS station should convert to a distance that approximately matches the water depth. A second (sometimes third) geometry definition and SEGY-conversion process was required until drift-corrections were found to match the expected direct travel time from water depth and closest airgun position to the "measured" direct arrival times. This iterative process is only an approximation, as the final OBS location on the seafloor has yet not been determined (see below Section 4 for details). The final OBS drift applied is listed together with the clock-drifts in Table 2.

4 Ocean Bottom Seismometer Relocation Analysis

The OBSs were deployed from the stern of the vessel and after release they fall to the seafloor at an approximate speed of 1 m/s. It cannot necessarily always be assumed that the instrument will descend straight down to the seafloor, due to currents within the water column. It is therefore important to carry out a relocation analysis of the instrument using the direct arrival times from the airgun shots to constrain the position. Most instruments were deployed in water depths of less than 100 m (Table 1) and only small drifts are expected. We use the relocation-algorithm *obsloc.m* provided by Prof. Dr. Keith Louden at Dalhousie University, to be used in MATLAB®. This algorithm uses ray-tracing based on a water-velocity profile. Through an iterative process, the best OBS location is defined that minimizes the misfit between the measured and calculated travel-times of the direct airgun arrivals. During Expedition ARA04C

several Conductivity-Temperature-Depth (CTD) profiles were measured, especially at two OBS stations (OBS-A, OBS-D) on the slope and shelf to calculate the sound speed in water (Figure 9).

Around each OBS station (except station OBS-L that was lost), direct arrival times were manually picked from the SEGY data. Where possible, data from all crossing lines were incorporated to improve on the position estimate and remove bias from a single 2D linear profile. In case of OBS-D no such relocation was performed, as the line was abandoned prior to arriving at the OBS location itself and multiple airgun failures resulted in no useful direct arrivals to be used in the relocation analysis. Some limited refraction data for a 1D velocity analysis was recorded for about 25 km along Line-22, but the deployment location has to be used for offset definition. Results of the re-location analysis are summarized graphically in Figures 10 – 16 and the relocated positions are listed in Table 1. Additional statistical information on the relocation analysis is listed in Table 3.

Initially, the OBS deployment sites were picked for regional coverage. Upon approaching the deployment site, the coincident acquisition of 3.5 kHz and multibeam data allowed for verification of the deployment spot to not be too close to an existing ice-scour. Although the footprint of the multibeam system in shallow water of ~70 m is relatively narrow (100 to 150 m), it is sufficient to detect any major ice-scours and their general orientation. As the drop-locations used in the relocation analysis were reported relative to the main GPS antenna of the vessel, a minimum drift equivalent to the distance between stern and GPS antenna are expected (i.e. 65 m).

As the re-location analysis has shown, the typical drift of an OBS is in the order of 50 to 70 m, well within the expected drift distance and the uncertainty of picking first arrivals on the OBS data. The two exceptions with apparent higher drift-distances are OBS-A (~140 m drift) and OBS-P (~100 m drift). In case of OBS-A, no data exist that go exactly across the OBS position and the azimuth coverage is biased to shots from the SE only. In case of OBS-P, an apparent artificial shift of 750 ms had to be applied to the data to bring the observed first arrival times within the traces around the intended OBS station to within +/-10 m of the expected water depths. Such a large shift arbitrarily applied to the data may be the reason for a larger drift than what is anticipated.

5 Estimation of Ocean Bottom Seismometer Geophone Orientation

A simple way to define the orientation of the horizontal geophone components on the seafloor is to generate plots of particle motion (hodograms) for portions of the data where the geophone is excited from different azimuths. For each OBS station, we generated particle motion diagrams from each direction with consistent azimuth for which a straight wave-front approach to the geophone can be assumed. The following naming convention is used for the seismic data:

- Channel 1: Hydrophone
- Channel 2: Vertical component (Z-axis)
- Channel 3: Horizontal component 1 (North, or Y-axis)
- Channel 4: Horizontal component 2 (East, or X-axis)

Typically, a 100 ms time window was used with an average of 10 traces for one particle motion diagram. The particle motion in the x-y plane resembles the shape of an ellipse; yet theoretically, in the absence of any noise, it would be a straight line. The first step in the calculation for the orientation is to rotate one hodogram (e.g. quadrant 1 or 3) so that particle motion would be only occurring along one of the axes, i.e. motion appears “flattened” in this rotated hodogram. Then this hodogram with the “flattened” arrival needs to be further rotated to be aligned to the azimuth of the shot-line direction to get the angle of the component relative to “true” North. The other component is then offset by 90º. As a quality control, one can rotate the hodogram in the adjacent quadrant by the angle required to “flatten” the first hodogram. The particle motion in the second hodogram is not flat, but at an angle equivalent to the difference in azimuth of the shot lines. An example: At station OBS-J, the particle motion in quadrant 1 and 3 appears to be about 45° (+/- 2°), measuring the angle in a clock-wise fashion. Rotating the hodogram clock-wise by this amount creates motion only along the N-axis (and no motion along the E-axis), i.e. the motion appears “flattened”. The particle motion in the opposite quadrants 2 and 4 is ~118° (+/- 2°). Applying a clock-wise rotation of 45° results in a modified hodogram, where the remaining particle motion is now at an angle of ~163°. In order to “flatten” this particle-motion and have only motion along the E-axis, a further rotation of 73° is required, which is close to the difference in azimuth of the seismic lines (reported to be 72°). Results from this preliminary analysis are summarized in Table 4, and graphical examples of the solutions are shown in Figures 17 – 23 for those OBS stations with more than two different shooting azimuths.

It is recognized that this technique is rather crude and heavily dependent on the time- and shot-window chosen by the interpreter and has therefore some uncertainty on the calculated orientation angle. More computational intensive approaches can be used, e.g. the approach suggested by Li and Ronen (2004). This technique was applied by Dash (2007) to OBS data from the Cascadia margin of the same OBS type as used in this Beaufort study. However, the technique by Li and Ronen (2004) works best for deep-water applications, where the first arrival is isolated from any refraction or converted-wave reflection arrivals. This is not the case in this Beaufort deployment and therefore, the routines by Li and Ronen (2004) were not utilized.

Instead, we have implemented the algorithm developed by Rosenberger (2010) for all OBS stations to verify the simple approach taken by the hodogram analyses. This algorithm detects the orientation of maximum motion in the vertical (z) direction and projects that onto the horizontal (x-y) plane. The angle of this projection to the y-axis is then used to calculate the OBS azimuth relative to true North. This algorithm does not rely on the relative motion of the two horizontal components (which is the approach taken with the hodograms above) and thus offers a second opinion on the OBS azimuth. The algorithm scans through the entire data sets (for the given shot range and time intervals provided by the user) and includes arrivals with inclination-angles between 0.3 and 0.99 (where the value '0' is perfectly horizontal motion, and the value '1' meaning perfectly vertical angle of incidence). In order for the (elliptical) particle motion detected to be incorporated in the analysis, the rectilinearity value (parameter $rect_{min}$ in Figure 24) has to be at a minimum of 0.6. Data within a time-window of 6 s (the parameter is referred to as L_T in Figure 24) is used in the calculation, and weighted by an exponential function as described in Rosenberger (2010).

The algorithm by Rosenberger (2010) produces a final histogram distribution of the residual angle between the orientation of the internal OBS axis and the shot azimuth, or, in other words, the angle of rotation required to move the internal OBS axes to true North (as report in Table 4). As this algorithm was initially developed for seismological applications, the code assumes that the direct incident P-wave comes from the sub-surface and has an upward motion. However, in the case of a marine OBS instrument, the direct P-wave through the water column creates a downward motion onto the geophone and the algorithm then creates an output that is rotated by 180º. Therefore, the resulting histogram distributions can include two solutions (offset by 180º) created by the arrivals through the water column and by the refracted arrivals from the

subsurface. The sign convention in the algorithm is such that negative azimuth values correspond to a counter-clockwise rotation of the OBS to align the N-axis (equivalently channel 3) to true North. In case of the station OBS-J, the algorithm by Rosenberger (2010) applied to shots from all four quadrants yields three solutions with corresponding uncertainties derived from the width of the histogram around the corresponding peak values (Figure 24). Two solutions are -93° (+/- 3.5°) and +84° (+/- 1.5°), which is about 180° offset from the first solution, and one additional solution is at -87° (+/- 3°), where the 180-phase rotated solution is minimal. The hodogram analysis of the two horizontal components in all four quadrants yields an average angle of 95° to be applied in a counter-clockwise rotation, which corresponds well with the results from the Rosenberger (2010) algorithm. All results are listed in Table 4.

Similar to the particle motion diagrams for the two horizontal components (x-y), such hodograms for the vertical and horizontal components (x-z, and y-z) can be created. Those will yield an estimate of the tilt angle of the OBS. For this analysis it is important to isolate a segment of data on the traces with the direct arrival of the airgun shot. Also, the horizontal components would have to be rotated based on the analysis described above. If a window is chosen that incorporates ground-roll or other type of noise, the geophone-response (particle motion) will not necessarily be useful to define the tilt of the instrument. In the Beaufort Sea experiment, almost all stations are in very shallow water (< 100 m) and therefore, the direct arrival through the water is almost immediately taken over by refractions. The horizontal rotation analysis described above is at this stage only a rough estimate and performed to get a general idea of the data validity and consistency of acquisition. The geometrically consistent (at least on a first order) results are encouraging for future analysis and at such a later stage, a more robust and complete particle-motion analysis, appropriate horizontal rotation, and tilt estimate should be performed.

6 Preliminary P-wave Velocity Analysis

Two examples of the OBS data acquired at OBS-F along seismic Line-8 and Line-5 are shown in Figure 32 and Figure 33, respectively. The data were processed only for visual inspection with a band-pass filter and an automatic gain control (AGC) window length of 500 ms. No data-rotations based on the above mentioned particle-motion diagrams were performed. The data on OBS-F show clear refractions seen over distances of 20 km until noise levels on the components becomes increasingly large for detecting the arrivals. The direct arrival is seen as a straight high frequency (80-100 Hz) arrival of hyperbolic shape (as expected). The refractions are generally of much lower frequency content (< 40 Hz) but can be clearly identified as straight-line arrivals on the traces. The first refraction that can be identified represents a velocity around 1800 m/s (or lower). The following refractions are often showing a velocity gradient, i.e. a gradual decrease in slope away from the OBS center-position. Some linear approximations to refractor-segments were used to define some velocity values and the results shown in Figure 32 and 33 show a gradual increase in sub-surface velocity from 1800 m/s, to values between 2000 m/s and 2500 m/s in a segment of distance 10 km away from the OBS stations, to values between 3500 m/s and 4000 m/s at 20 km distance. Some reflections are also clearly visible and can be exploited for velocity analyses, but this requires a ray-tracing based inversion approach, not yet conducted.

References

Dallimore, S.R., Paull, C.K., Collett, T.S., Jin, Y.K., Mienert, J., Mangelsdorf, K., Riedel, M., 2012. Drilling to investigate methane release and geologic processes associated with warming permafrost and gas hydrate deposits beneath the Beaufort Sea Shelf. IODP Pre-Proposal 806, available online at http://iodp.org/

Dash, R.K., 2007. Crustal Structure and Marine Gas Hydrate Studies near Vancouver Island using Seismic Tomography, PhD thesis, University of Victoria, Victoria, BC, Canada, pp 171.

Hu, K., Issler, D.R., Chen, Z., Brent, T.A., 2013. Permafrost investigation by well logs, and seismic velocity and repeated shallow temperature surveys, Beaufort-Mackenzie Basin, Geological Survey of Canada, Open File 6956, 2013; 33 pages, doi:10.4095/293120.

Li, J., S. Jin, and S. Ronen, 2004. Data-driven tilt angle estimation of multi-component receivers, in 74th Ann. Internat. Mtg., Expanded Abstracts, Soc. Expl. Geophys, MC3.5.

O'Regan, M., de Vernal, A., Hill, P., Hillaire-Marcel, C., Jakobsson, M., Moran, K., Rochon, A., St-Onge, G., 2010. Late quaternary paleoceanography and glacial dynamics in the Beaufort Sea, IODP pre-proposal #753, available online at http://iodp.org/.

Pullan, S., MacAulay, M.H., Hunter, J.A.M., Good, R.I., Gagne, R.M., Burns, R.A., 1987. Permafrost distribution determined from seismic refraction, in: Marine Science Atlas of the Beaufort Sea: Geology and Geophysics, ed. by B.R. Pelletier, Geological Survey of Canada Miscellaneous Report 40.

Rosenberger, A. 2010. Realtime Ground-Motion Analysis: Distinguishing P and S Arrivals in a Noisy Environment, Bull. Seism. Soc. Am., 100, 1252-1262.

OBS-ID	Original Position		Relocation		Water depth (m)
	Latitude	Longitude	Latitude	Longitude	
OBS-A	70°39.8856	135°45.8101	70º 39.8335	-135º 45.9708	254
OBS-E	70°36.4466	135°37.7178	70º 36.4735 *(70º 36.4495)*	-135º 37.7186 *(-135º 37.8148)*	74
OBS-F	70°30.9717	135°25.0372	70º 30.9933 *(70º 30.9994)*	-135º 24.9893 *(-135º 24.9734)*	64
OBS-H	70°23.1932	135°07.4192	70º 23.2254 *(70º 23.5032)*	-135º 7.4834 *(-135º 7.6825)*	57
OBS-J	70°26.5783	134°42.5861	70º 26.60532 *(70º 26.0860)*	-134º 42.666 *(-134º 43.4323)*	55
OBS-K	70°33.7002	134°59.4760	70º 33.7002 *(70º 33.6785)*	-134º 59.55678 *(-134º 59.5420)*	57
OBS-D	70°45.3078	134°09.3476	n.p.		68
OBS-L*	70°45.2910	134°09.2436	n.p.		67
OBS-P	70°36.2777	133°48.2597	70º 30.0042 *(70º 29.9966)*	-133º 33.9483 *(-133º 33.9785)*	68

Table 1. OBS stations deployed during expedition ARA04C. Locations from the re-location analysis yielded conjugate positions for the OBS, which statistically are as valid as the primary solution. The conjugate values are (when they could not be excluded as in Case of OBS-A) shown in parentheses and italics. See Table 3 for additional parameters of the re-location analysis. (*: Station was not recovered; n.p. not processed).

OBS-ID	Clock drift (msec)	Additional delay (msec) applied
OBS-A	+5.623	-100
OBS-E	-29.45	-100
OBS-F	+22.227	-100
OBS-H	+17.676	-100
OBS-J	+5.901	-100
OBS-K	-45.584	-100
OBS-D	+22.86	-100
OBS-P	+0.647	-750

Table 2. OBS drift-time correction. Complete information on the clock drift-parameters is given in the Appendix.

OBS-ID	Maximum range used in inversion and increment (m)	Number of traces used	Total drift for best-fit OBS position (m)	Final rms misfit (sec)
OBS-A	12000 / 100	115	141.4	0.02953
OBS-E	1500 / 50	30	50.0	0.00820
OBS-F	1000 / 10	34	50.0	0.065485
OBS-H	4000 / 20	127	72.1	0.02174
OBS-J	6000 / 50	158	70.7	0.02631
OBS-K	12000 / 50	294	50.0	0.028921
OBS-D	n.p.			
OBS-P	7000 / 50	72	103	0.011979

Table 3. Statistical information on OBS relocation analysis (n.p.: not performed).

OBS-ID	**OBS azimuth (°)** Hodogram	**OBS azimuth (°)** Rosenberger (2010)	**Average OBS azimuth (°)**
OBS-A	33 *(Figure 22, quad. 2)* 30 *(Figure 22, quad. 3)*	-32 (+/-4)	31.5
OBS-E	~36 *(Figure 17, quad. 1)* 36 *(Figure 17, quad. 3)* 35 *(Figure 17, quad. 4)*	+147 (+/-4) (equiv. to -33)	35
OBS-F	125 *(Figure 18, quad. 1)* 120 *(Figure 18, quad. 2)* 114 *(Figure 18, quad. 4)* 125 *(Figure 18, quad. 3)*	+56 (+/-2) (equiv. to -124) +49 (+/-5) (equiv. to -131)	123
OBS-H	43 *(Figure 19, quad. 1)** 80 *(Figure 19, quad. 2)* 46 *(Figure 19, quad. 3)** 79 *(Figure 19, quad. 4)*	-77 (+/- 2.5) *(Figure 28a)*	79
OBS-J	93 *(Figure 20, quad. 2)* 96 *(Figure 20, quad. 2)* 95 *(Figure 20, quad. 3)* 97 *(Figure 20, quad 4.)*	-87 (+/-3)	93.5
OBS-K	29 *(Figure 21, quad 1.)* 24 *(Figure 21, quad 2.)* 19 *(Figure 21, quad 3.)** 24 *(Figure 21, quad 4.)*	+155 (+/- 2) (equiv. to -25) +156 (+/- 2.5) (equiv. to -26)	25.5
OBS-D	81 (Figure 23)	inconclusive	81
OBS-P	n.p.	+124 (+/-1.5)	+124

Table 4. Estimates of the OBS orientation using as reference the angle of the horizontal component 2 (defined as channel 3, y-axis) based on the analyses of particle motion diagrams shown in Figures 17 – 23, compared to solutions from the Rosenberger (2010) analysis. Note, the Rosenberger (2010) convention is that negative angles represents the angle required for counter-clock-wise rotation back to North; it also carries a 180º ambiguity. [*: not used in averaging]

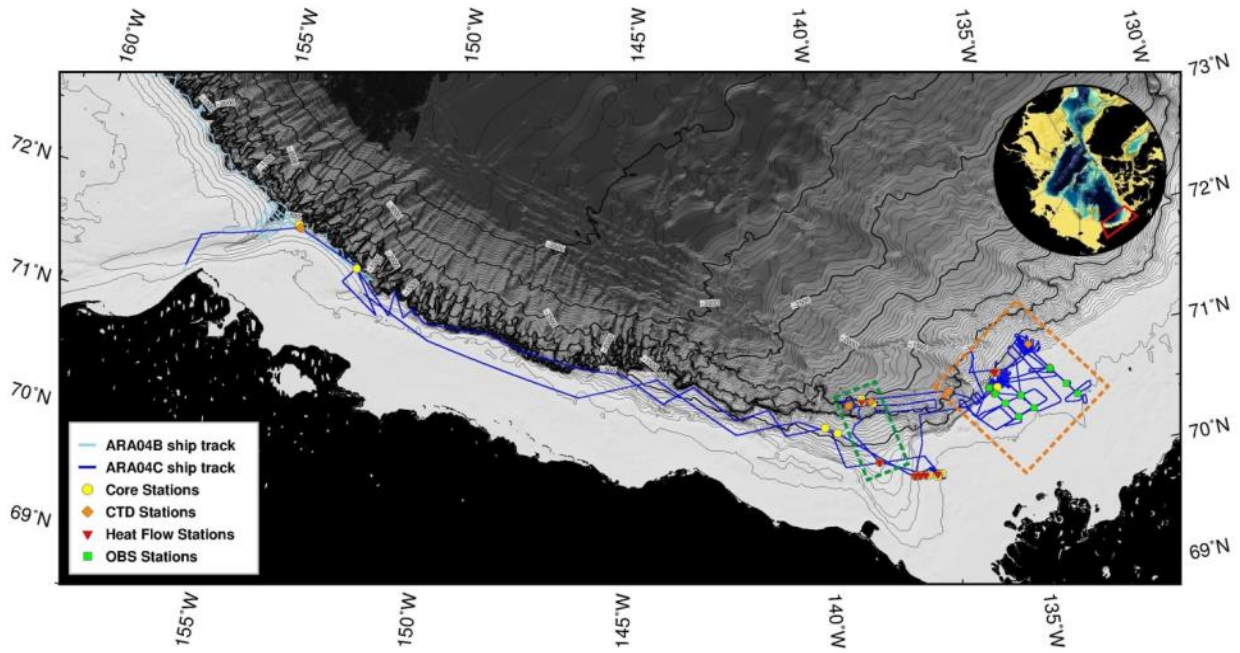

Figure 1. Overview map of the ship track for Expedition ARA04C. The expedition is split into two parts: September 6 - 9, 2013 in Alaskan waters off Barrow, and September 10 – 24, 2013 in Canadian waters off the Mackenzie Delta shelf and slope region. The small green box defines the region for IODP pre-proposals 753 (O'Regan et al., 2010) and the orange box defines the research region for IODP pre-proposal 806 (Dallimore et al., 2012).

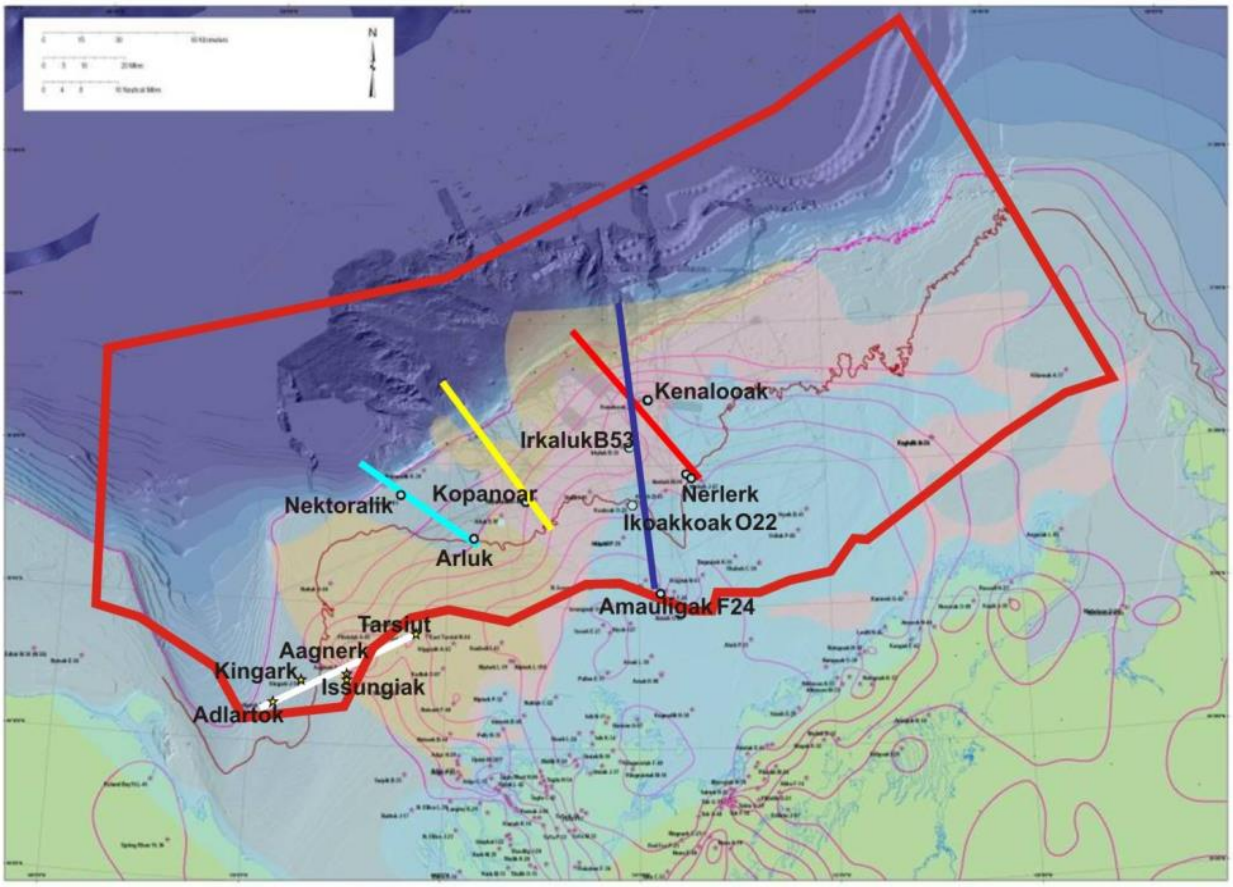

Figure 2. Location map of five main transects selected for regional characterization of permafrost distribution based on selected industry well sites. In order of priority, the transects are "red", "yellow" "blue", "cyan", and "white". The map shows in red the outline of the area of the permit for Expedition ARA04C, regions of permafrost occurrences after Pullan et al. (1987). Contour-lines are defining depth of permafrost as determined from temperature data acquired at industry well sites. The 100 m isobaths line is shown in pink, and the 50 m isobaths line (southern limit of permit for using the 1200 in^3 airgun array) is shown in brown.

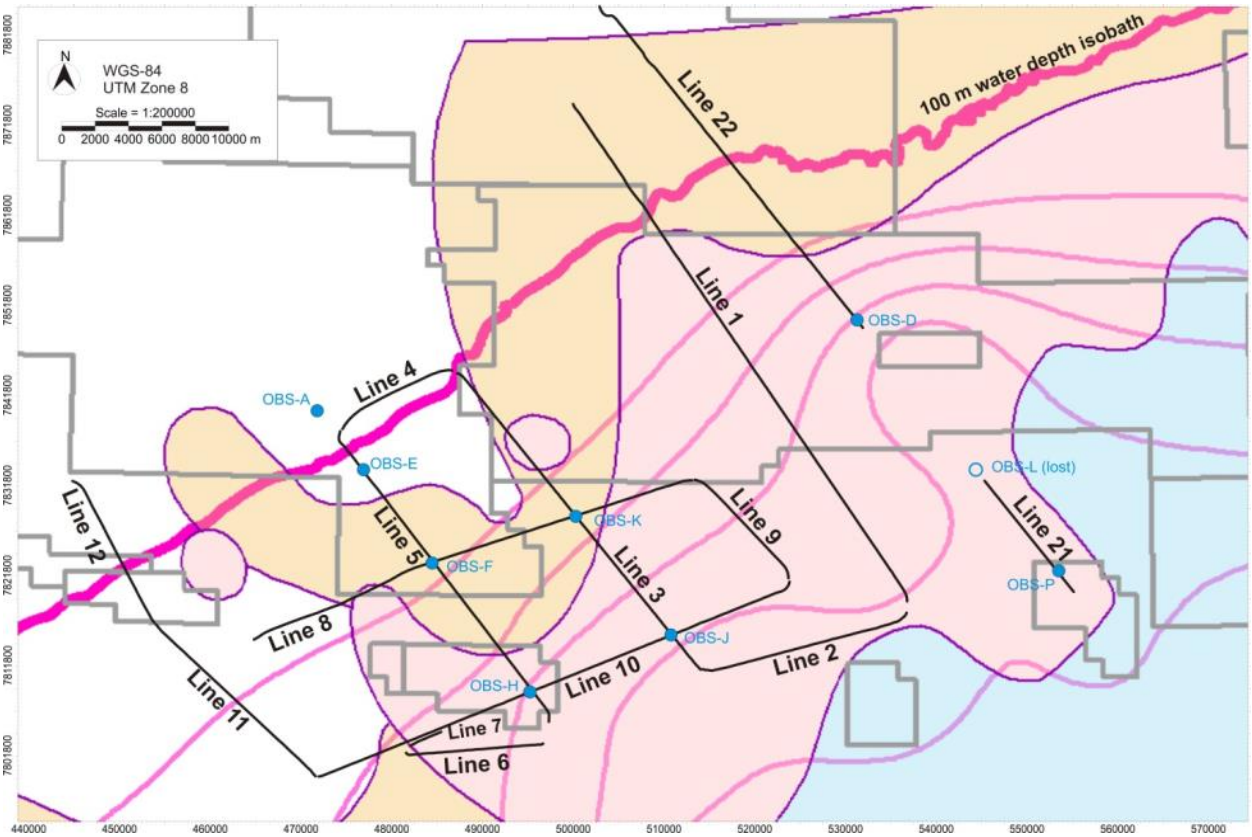

Figure 3. Layout of the Ocean Bottom Seismometer (OBS) stations (blue symbols) and orientation of the 14 seismic survey lines acquired.

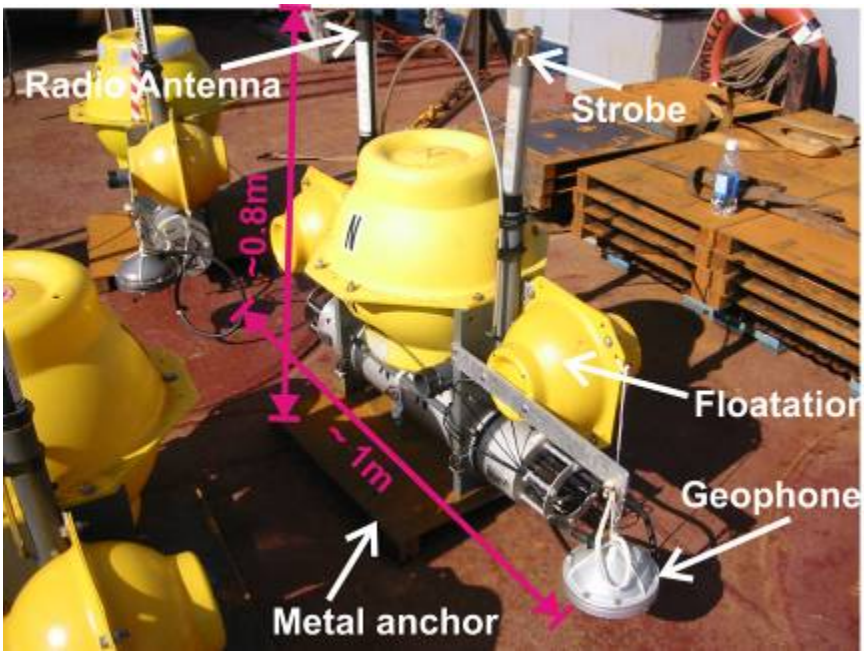

Figure 4. Image of a fully assembled OBS on deck.

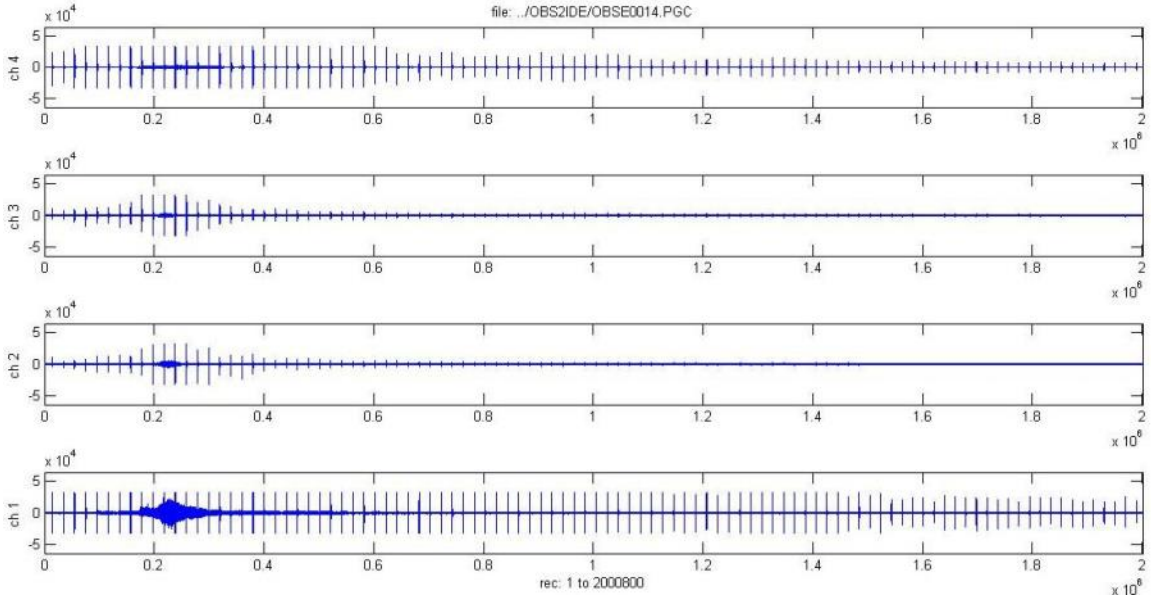

Figure 5. Example of seismic records using the onboard quick-check algorithm for OBS-E (Station ARA04C_14OBS001) showing regular airgun arrivals on all channels: Ch1= hydrophone, Ch2 = vertical geophone component, Ch3/4 = horizontal geophone components. The time when the Araon is directly over the OBS-E location can be seen by the increase in high frequency noise on the hydrophone data.

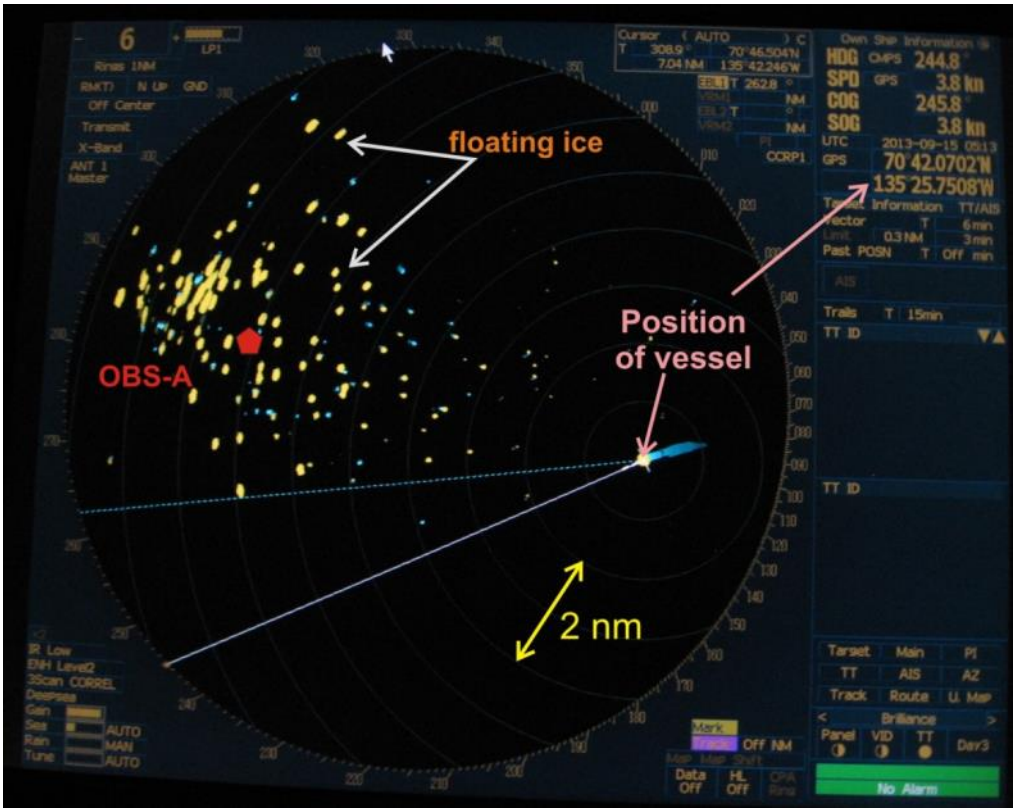

Figure 6. Screenshot of the ship's radar showing location of OBS-A (station ARA04C_13OBS_001) relative to the Araon, which deflected the line orientation for seismic data acquisition. Floating ice (seen as yellow radar reflectors on the screen) is covering the OBS location and it would have been impossible to tow the airgun array and streamer through those ice-infested waters. Therefore, no direct crossing of station OBS-A was completed. The cumulative motion of individual radar-reflectors is seen on the screen as blue "shadows" (e.g. the blue line behind the vessel's position, or small blue lines behind individual ice-pieces). In this case, the maximum motion of the ice pieces was generally towards the SW (towards the OBS station) at a speed of ~1/20 of a nautical mile over 10 minutes (equivalent to ~10 cm/s).

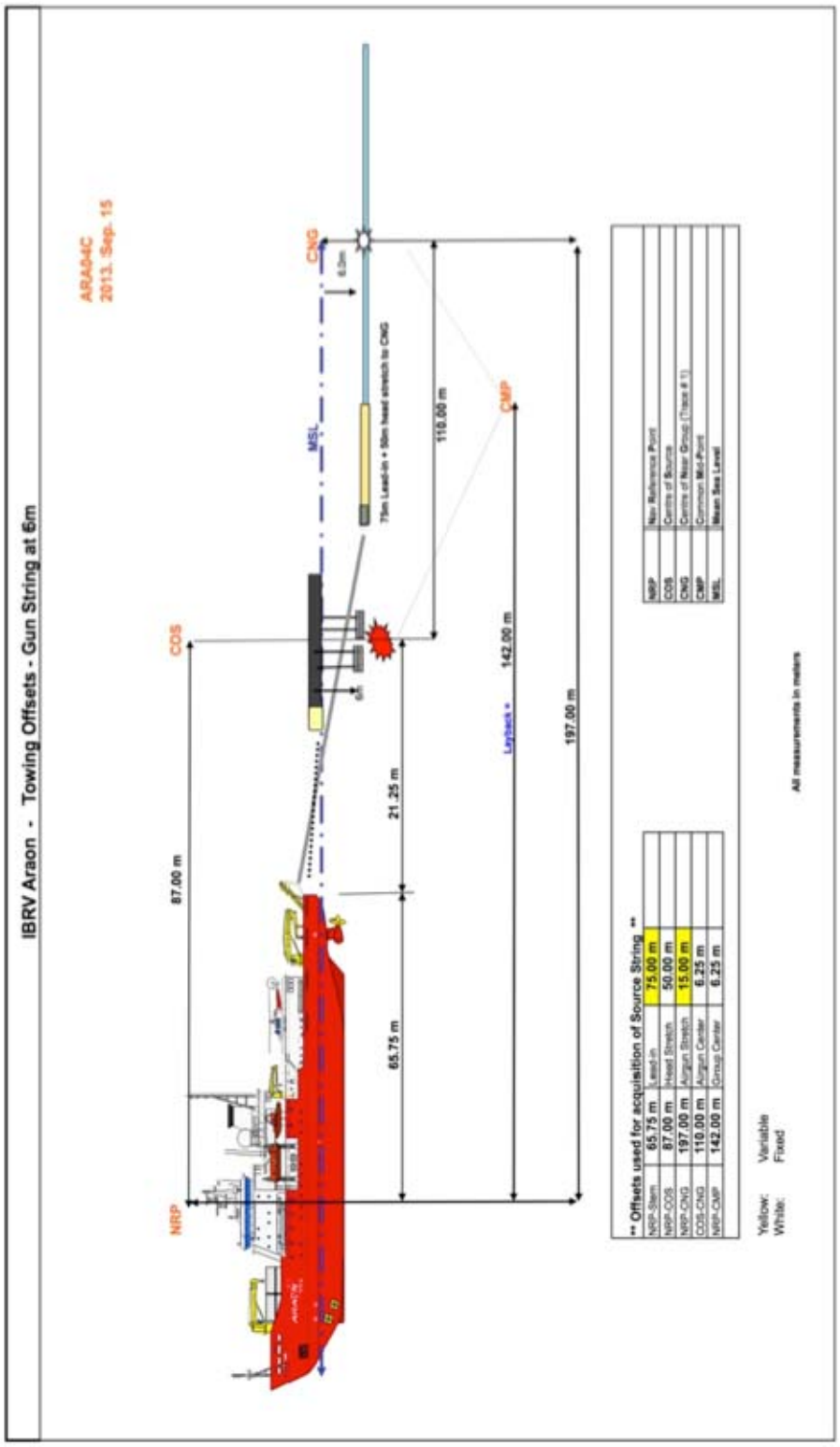

Figure 7. Offset information for the seismic survey and definition of distances between ship, airgun source, and streamer.

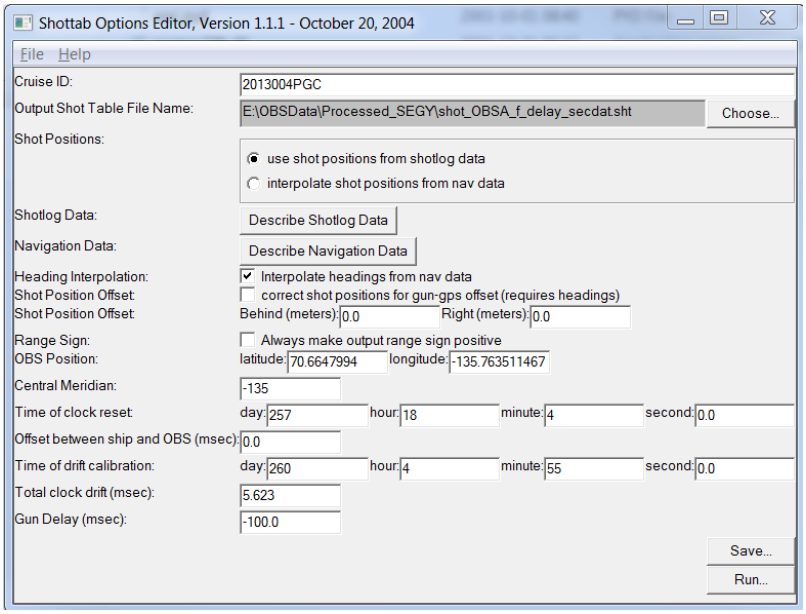

Figure 8. Screen-capture of the graphical user interface for the ShotTab software used to define initial (and re-located) geometry for each OBS.

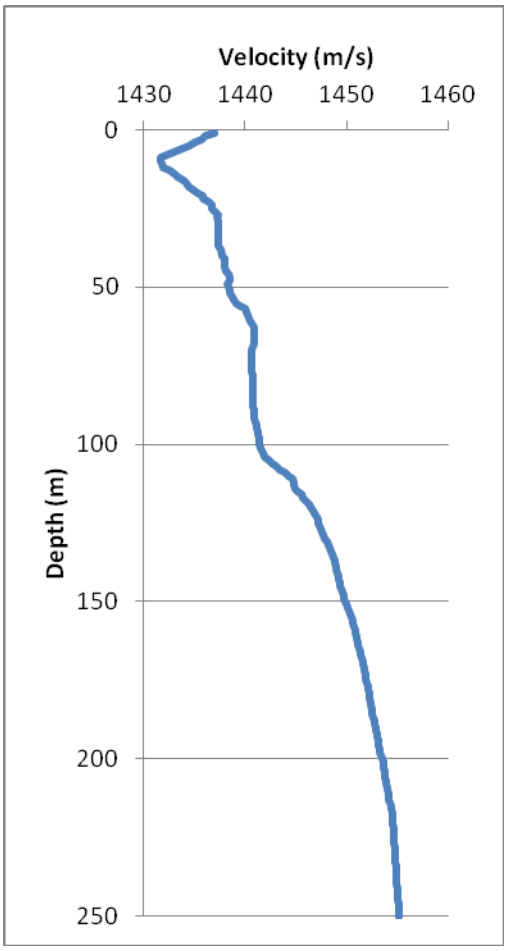

Figure 9. Sound-velocity profile on the shelf of the Beaufort Sea (at station OBS-D). A thin low-velocity zone near the sea surface is prominent.

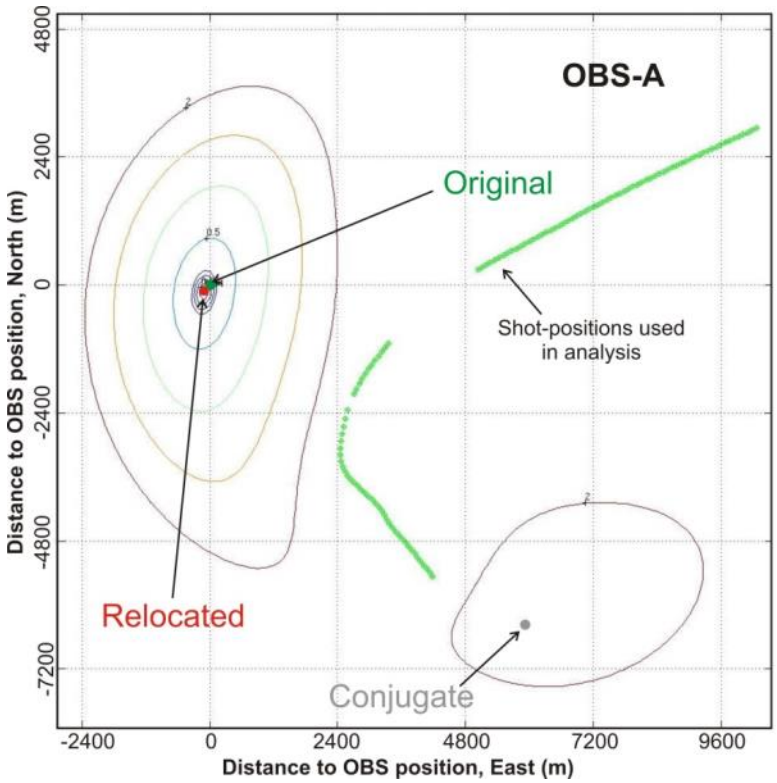

Figure 10. Graphical representation of the results from the relocation analysis of OBS-A. Contours represent OBS positions with a constant misfit between computed and measured arrival times (in sec). Original OBS position is shown in green, relocated OBS position is in red, and conjugate OBS position is in grey. All shots used in the analysis are shown as small green dots. The conjugate position was excluded as not possible, as the horizontal drift up-slope would be unrealistically large (>5 km where water depths are < 250 m).

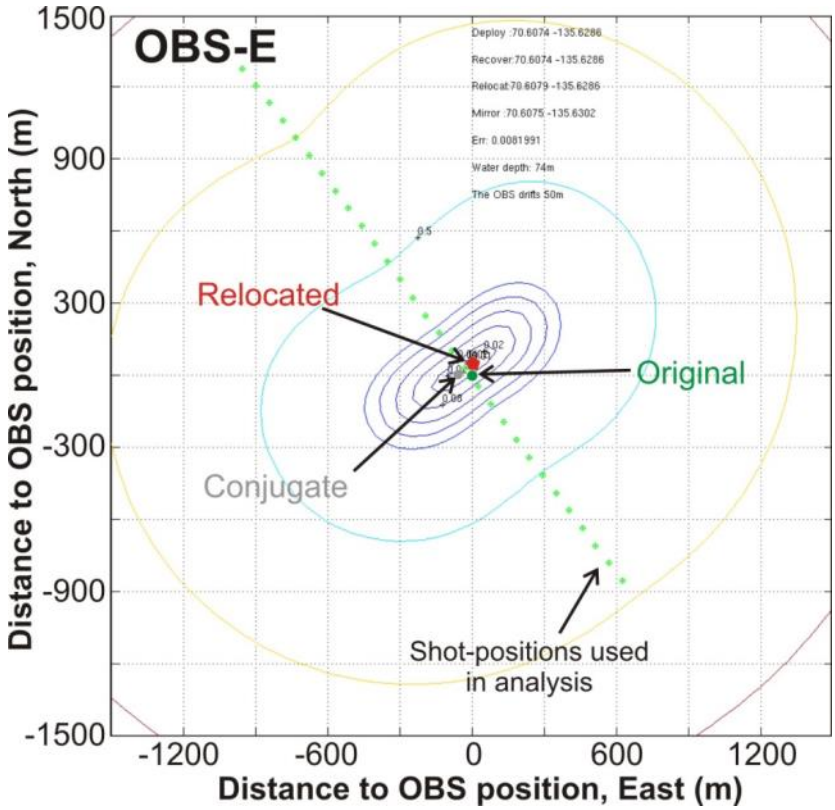

Figure 11. Graphical representation of the result of the relocation analysis for OBS-E. Contours represent OBS positions with a constant misfit between computed and measured arrival times (in sec). Original OBS position is shown in green, relocated OBS position is in red, and conjugate OBS position is in grey. All shots used in the analysis are shown as small green dots.

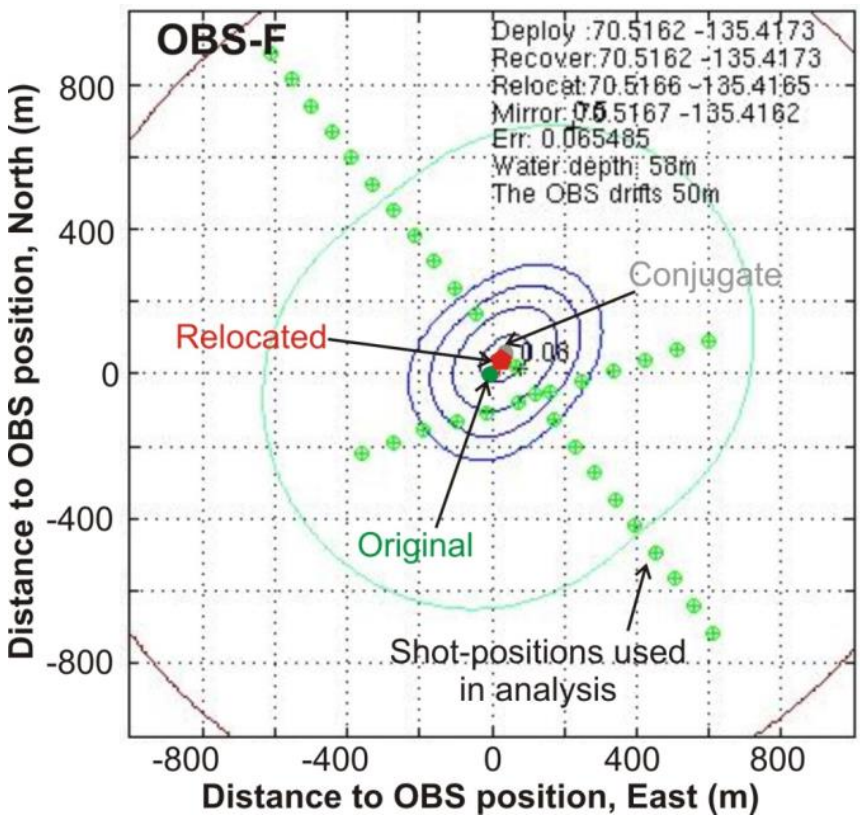

Figure 12. Graphical representation of the result of the relocation analysis for OBS-F. Contours represent OBS positions with a constant misfit between computed and measured arrival times (in sec). Original OBS position is shown in green, relocated OBS position is in red, and conjugate OBS position is in grey. All shots used in the analysis are shown as small green dots.

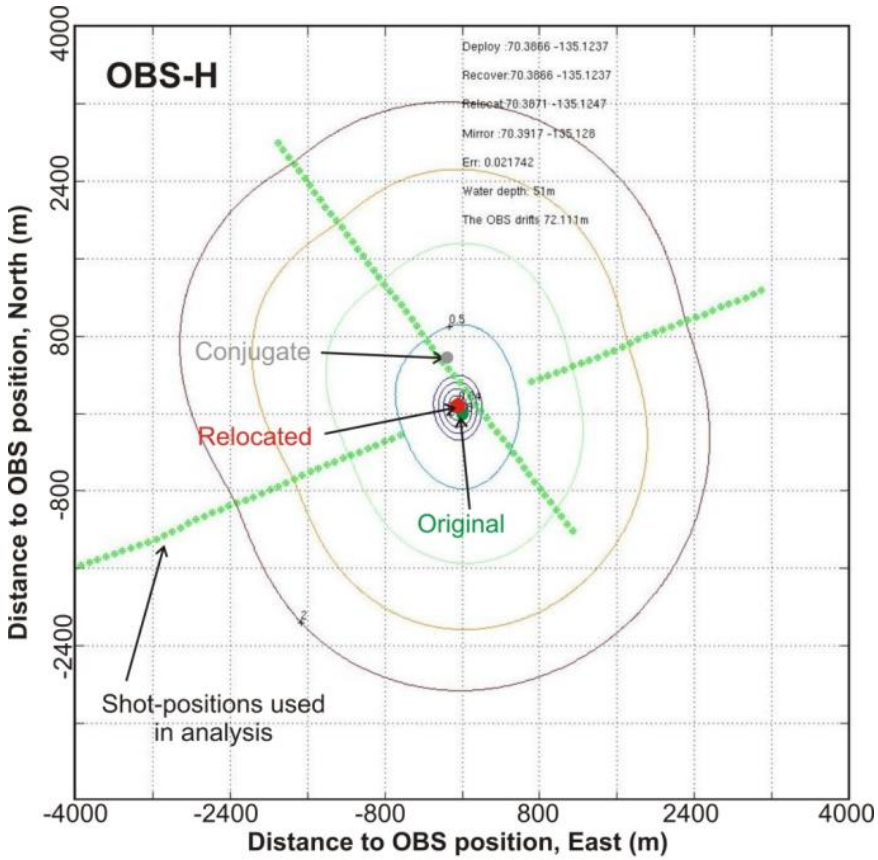

Figure 13. Graphical representation of the result of the relocation analysis for OBS-H. Contours represent OBS positions with a constant misfit between computed and measured arrival times (in sec). Original OBS position is shown in green, relocated OBS position is in red, and conjugate OBS position is in grey. All shots used in the analysis are shown as small green dots.

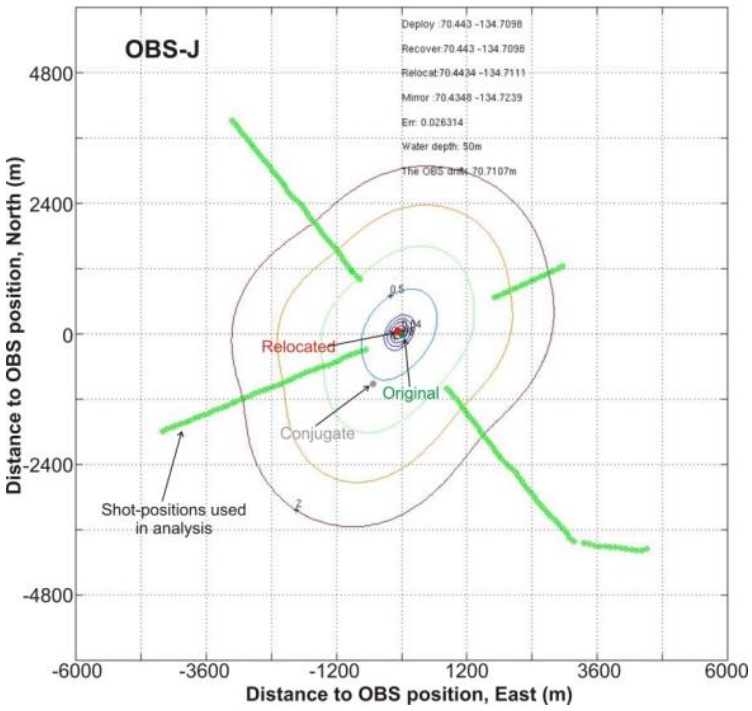

Figure 14. Graphical representation of the result of the relocation analysis for OBS-J. Contours represent OBS positions with a constant misfit between computed and measured arrival times (in sec). Original OBS position is shown in green, relocated OBS position is in red, and conjugate OBS position is in grey. All shots used in the analysis are shown as small green dots.

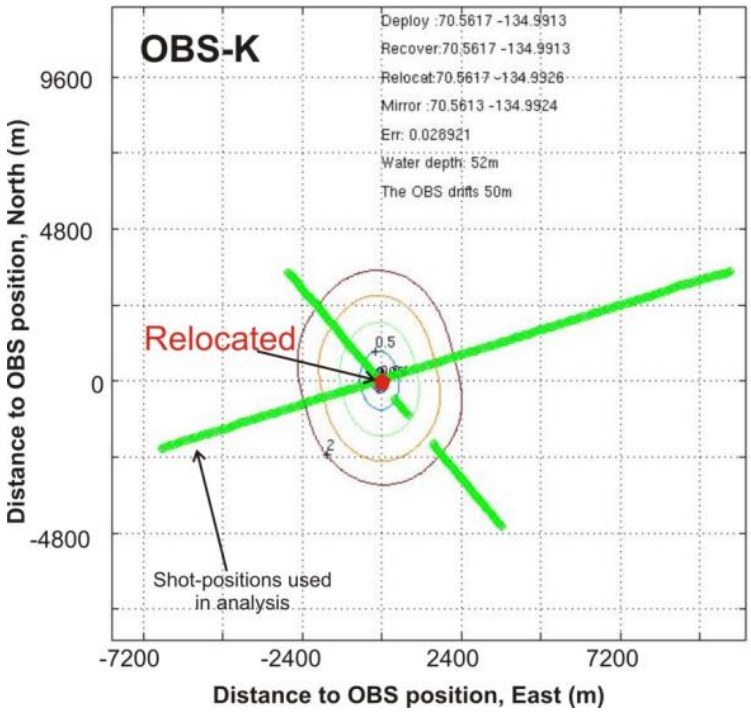

Figure 15. Graphical representation of the result of the relocation analysis for OBS-K. Contours represent OBS positions with a constant misfit between computed and measured arrival times (in sec). Relocated OBS position is in red. All shots used in the analysis are shown as small green dots.

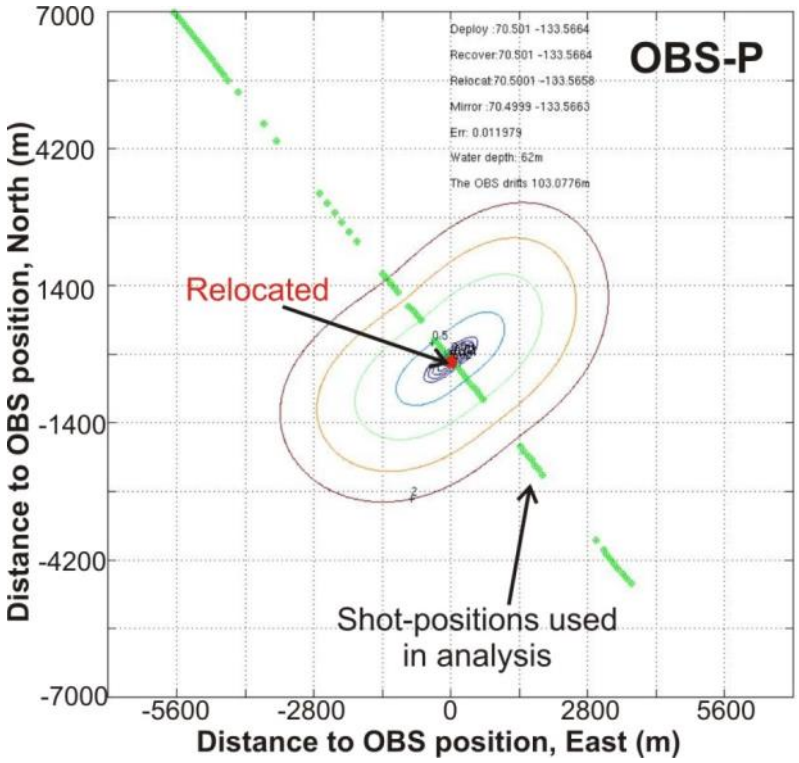

Figure 16. Graphical representation of the result of the relocation analysis for OBS-P. Contours represent OBS positions with a constant misfit between computed and measured arrival times (in sec). Relocated OBS position is in red. All shots used in the analysis are shown as small green dots.

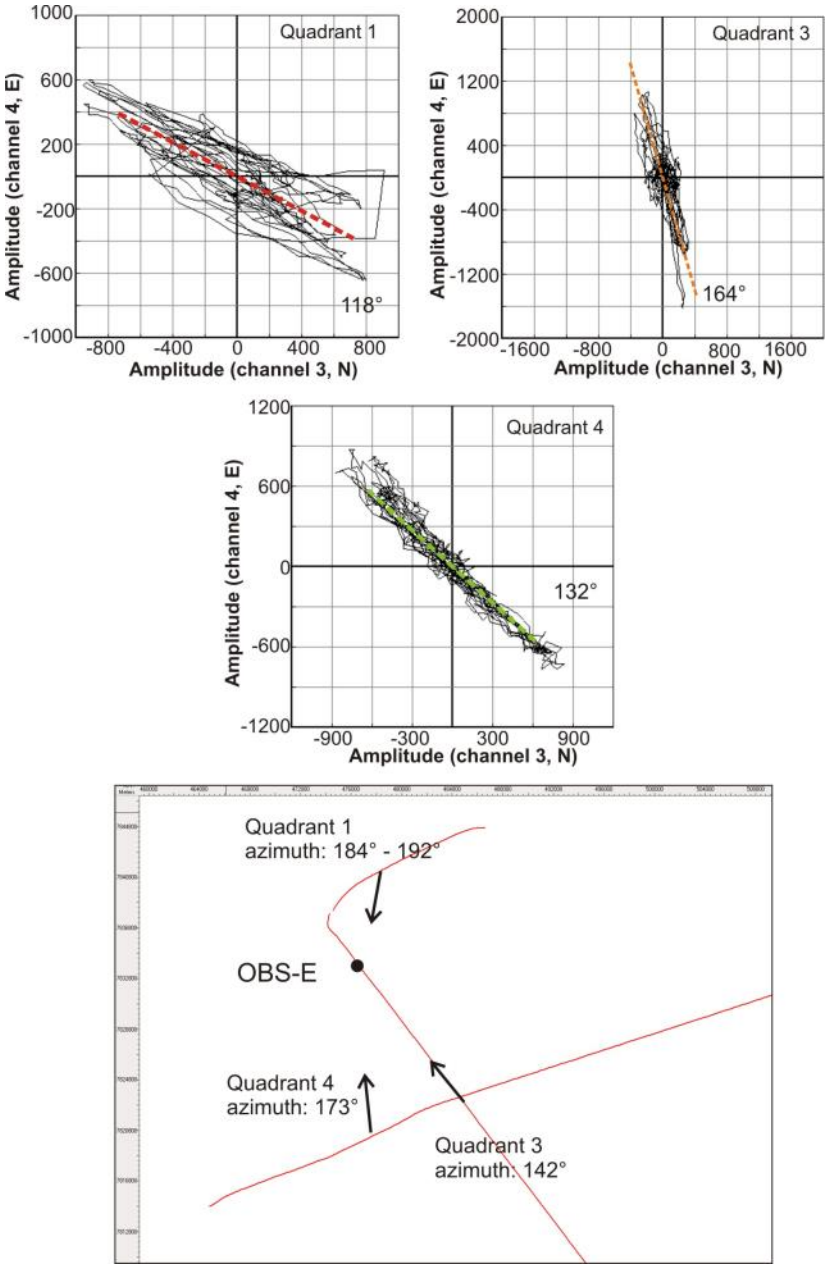

Figure 17. Simple analysis of particle motion diagrams of OBS-E to define OBS orientation on seafloor. The map shows the seismic lines acquired around the OBS station. The analysis is split into four quadrants with four different (but internally consistent) shooting-azimuths. Three particle motion diagrams are shown together with a best-fit line for the average motion on the components. Note: channel 3 of the OBS (horizontal component 1) is plotted on the horizontal-axis, and channel 4 of the OBS (horizontal component 2) is plotted on the vertical-axis with an equal-distance axes range.

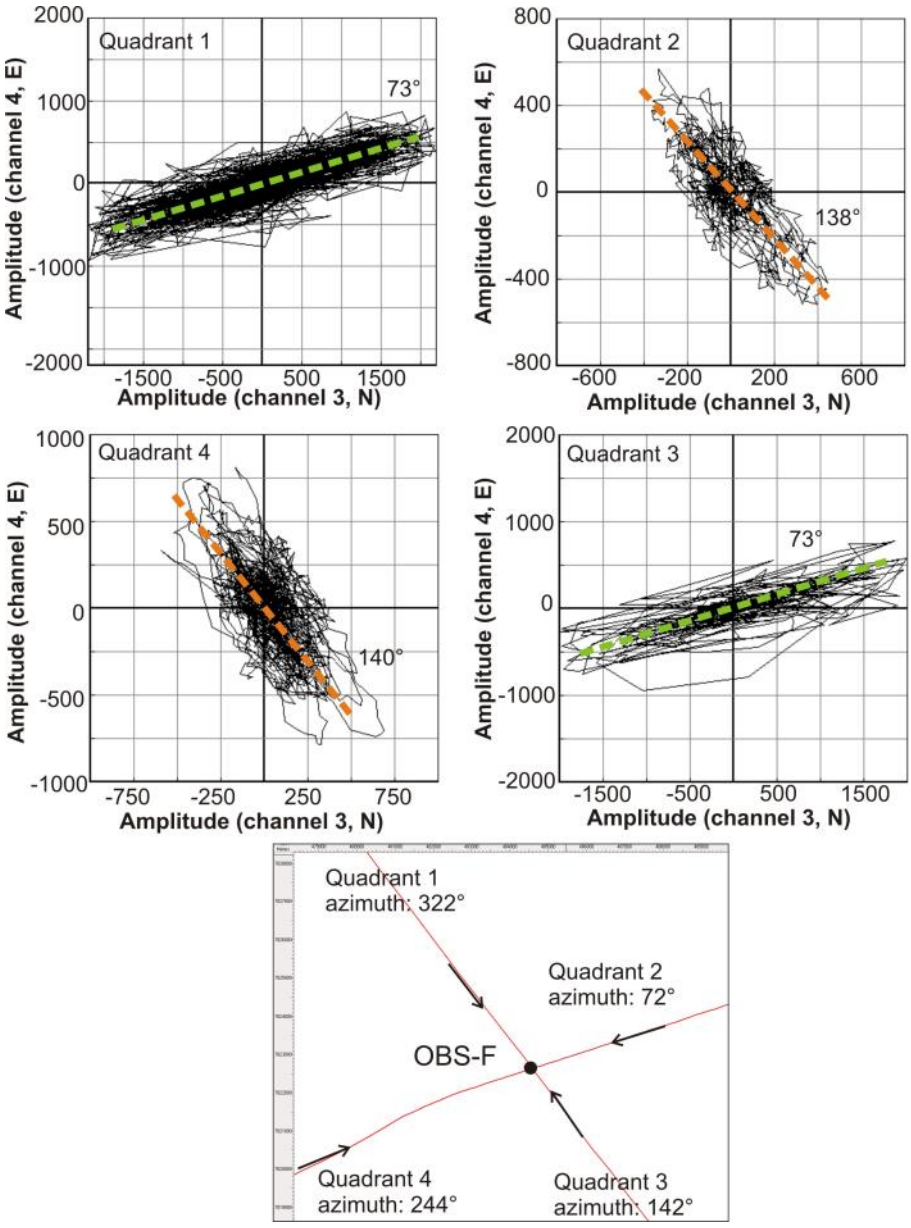

Figure 18. Simple analysis of particle motion diagrams of OBS-F to define OBS orientation on seafloor. The map shows the seismic lines acquired around the OBS station. The analysis is split into four quadrants with 4 different (and consistent) shooting-azimuths. The four particle motion diagrams representing these quadrants are shown together with a best-fit line for the average motion on the components. Note: channel 3 of the OBS (horizontal component 1) is plotted on the horizontal-axis, and channel 4 of the OBS (horizontal component 2) is plotted on the vertical-axis with an equal-distance axes range

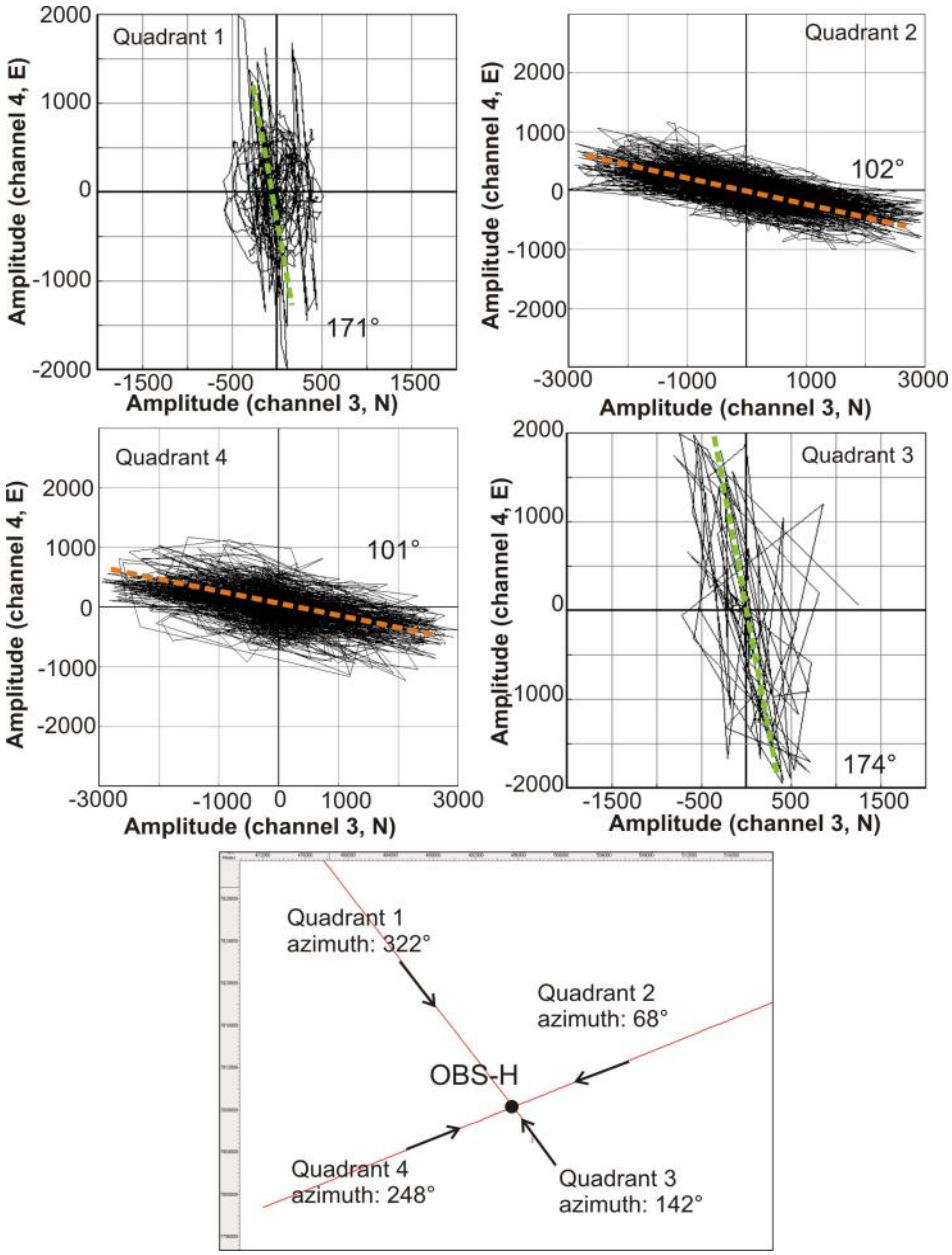

Figure 19. Simple analysis of particle motion diagrams of OBS-H to define OBS orientation on seafloor. The map shows the seismic lines acquired around the OBS station. The analysis is split into four quadrants with 4 different (and consistent) shooting-azimuths. The four particle motion diagrams representing these quadrants are shown together with a best-fit line for the average motion on the components. Note: channel 3 of the OBS (horizontal component 1) is plotted on the horizontal-axis, and channel 4 of the OBS (horizontal component 2) is plotted on the vertical-axis with an equal-distance axes range. Solutions for quadrant 1 and 3 are very noisy (compare to Figure 28b).

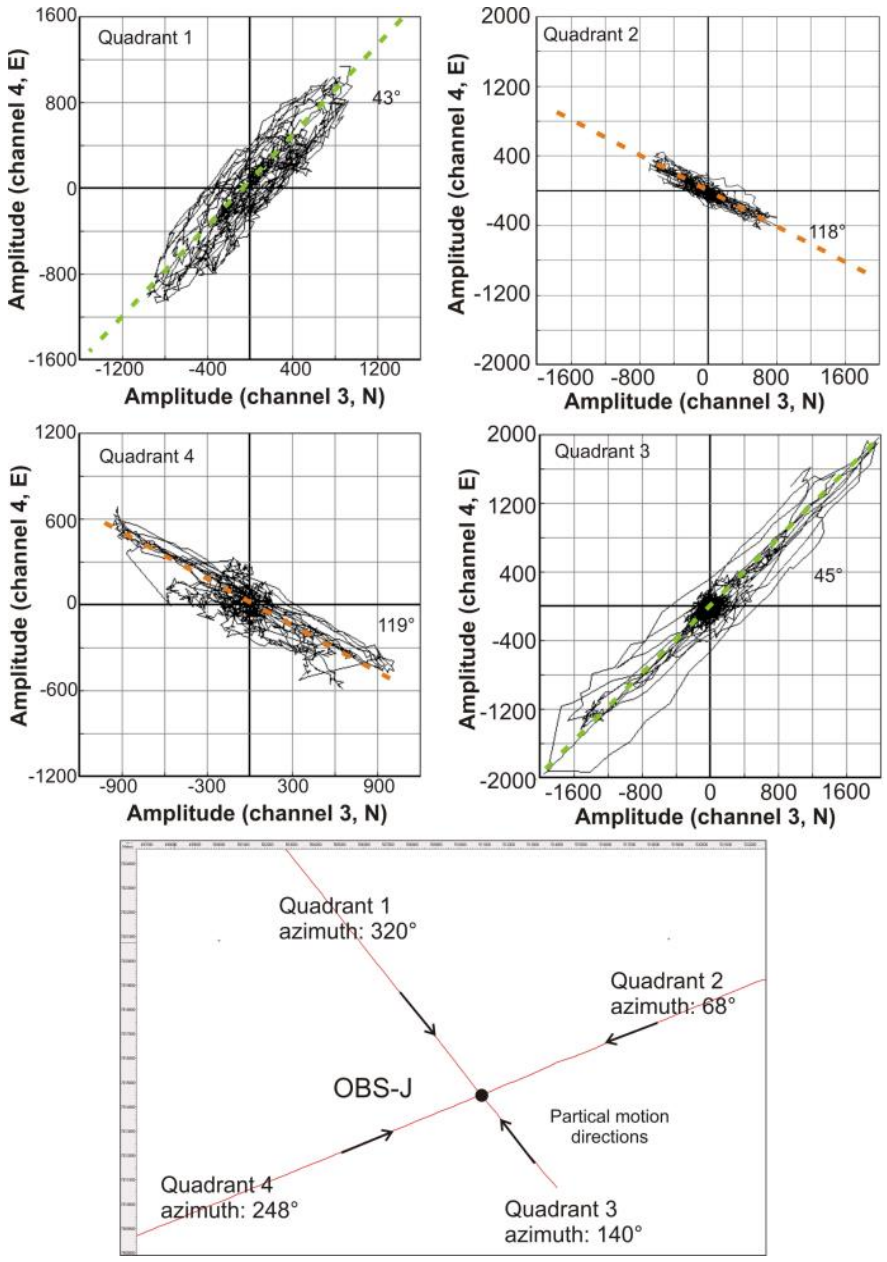

Figure 20. Simple analysis of particle motion diagrams of OBS-J to define OBS orientation on seafloor. The map shows the seismic lines acquired around the OBS station. The analysis is split into four quadrants with 4 different (and consistent) shooting-azimuths. The four particle motion diagrams representing these quadrants are shown together with a best-fit line for the average motion on the components. Note: channel 3 of the OBS (horizontal component 1) is plotted on the horizontal-axis, and channel 4 of the OBS (horizontal component 2) is plotted on the vertical-axis with an equal-distance axes range.

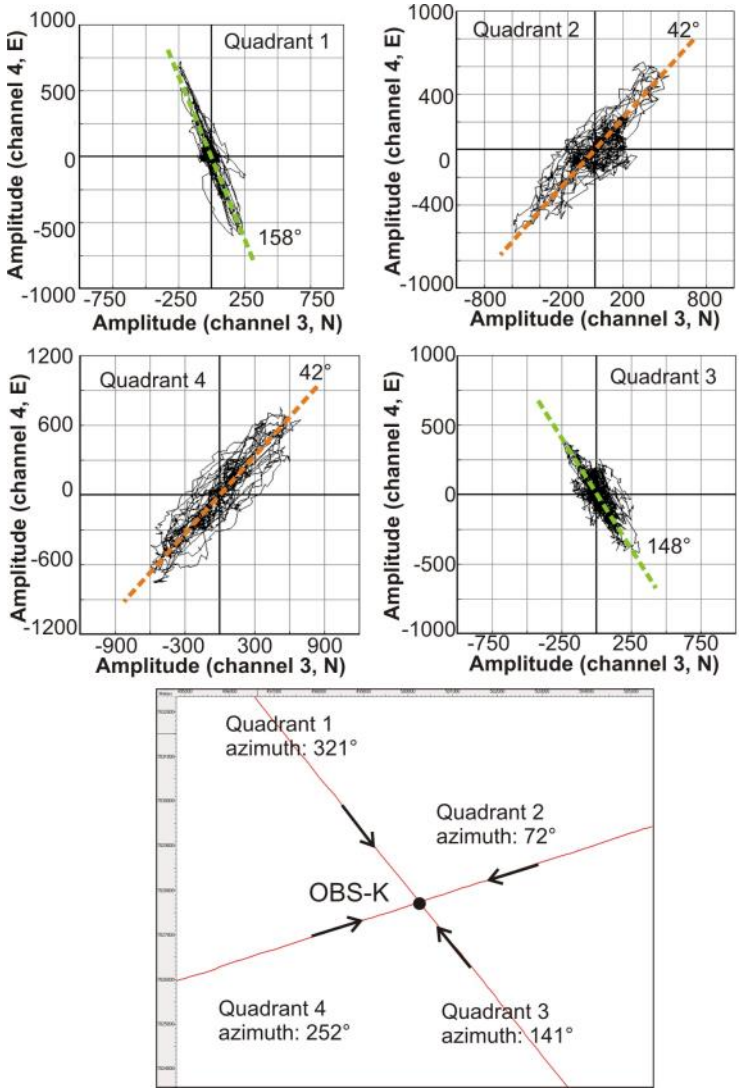

Figure 21. Simple analysis of particle motion diagrams of OBS-K to define OBS orientation on seafloor. The map shows the seismic lines acquired around the OBS station. The analysis is split into four quadrants with 4 different (and consistent) shooting-azimuths. The four particle motion diagrams representing these quadrants are shown together with a best-fit line for the average motion on the components. Note: channel 3 of the OBS (horizontal component 1) is plotted on the horizontal-axis, and channel 4 of the OBS (horizontal component 2) is plotted on the vertical-axis with an equal-distance axes range.

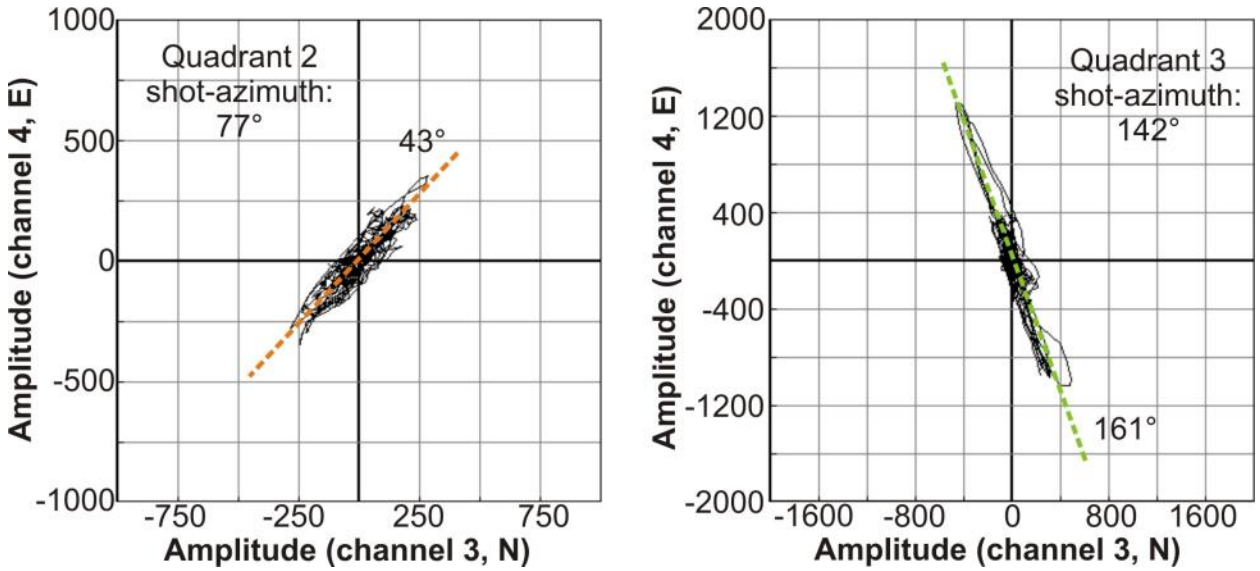

Figure 22. Simple analysis of particle motion diagrams of OBS-A to define OBS orientation on seafloor. The analysis is split into two quadrants with two different shooting-azimuths. The particle motion diagrams representing these quadrants are shown together with a best-fit line for the average motion on the components. Note: channel 3 of the OBS (horizontal component 1) is plotted on the horizontal-axis, and channel 4 of the OBS (horizontal component 2) is plotted on the vertical-axis with an equal-distance axes range. Quadrant 2: clockwise rotate by 47° to align motion to y-axis, then rotate counter-clockwise by 77° to align with true North, thus the OBS azimuth is at 30°; Quadrant 3: counter-clockwise rotation by 71° to align motion to y-axis, then 142° counter-clockwise rotation to align to true North, thus OBS azimuth is at 213° or equivalently 33°.

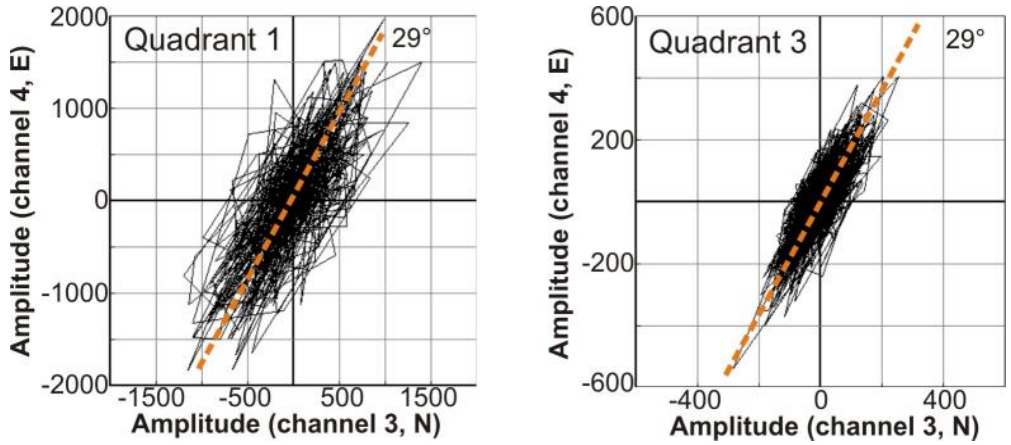

Figure 23. Simple analysis of particle motion diagrams of OBS-D to define OBS orientation on seafloor. The analysis is split into two quadrants with two different (and consistent) shooting-azimuths; only one line was acquired across this OBS in a general NW-SE direction. The particle motion diagrams representing these quadrants are shown together with a best-fit line for the average motion on the components. Note: channel 3 of the OBS (horizontal component 1) is plotted on the horizontal-axis, and channel 4 of the OBS (horizontal component 2) is plotted on the vertical-axis with an equal-distance axes range.

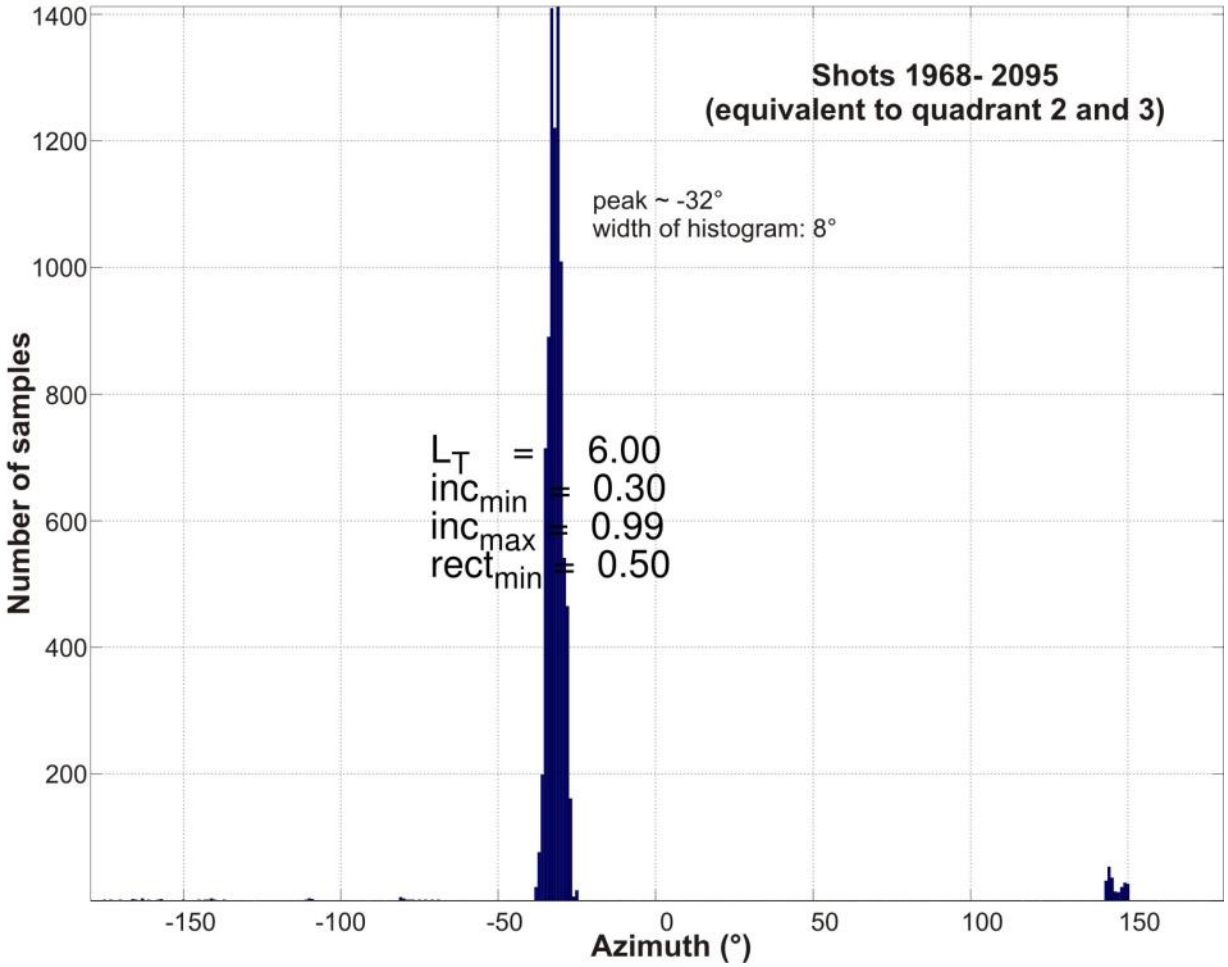

Figure 24. Results of the application of the Rosenberger (2010) azimuth-detection algorithm for station OBS-A (compare to Figure 22), details see text.

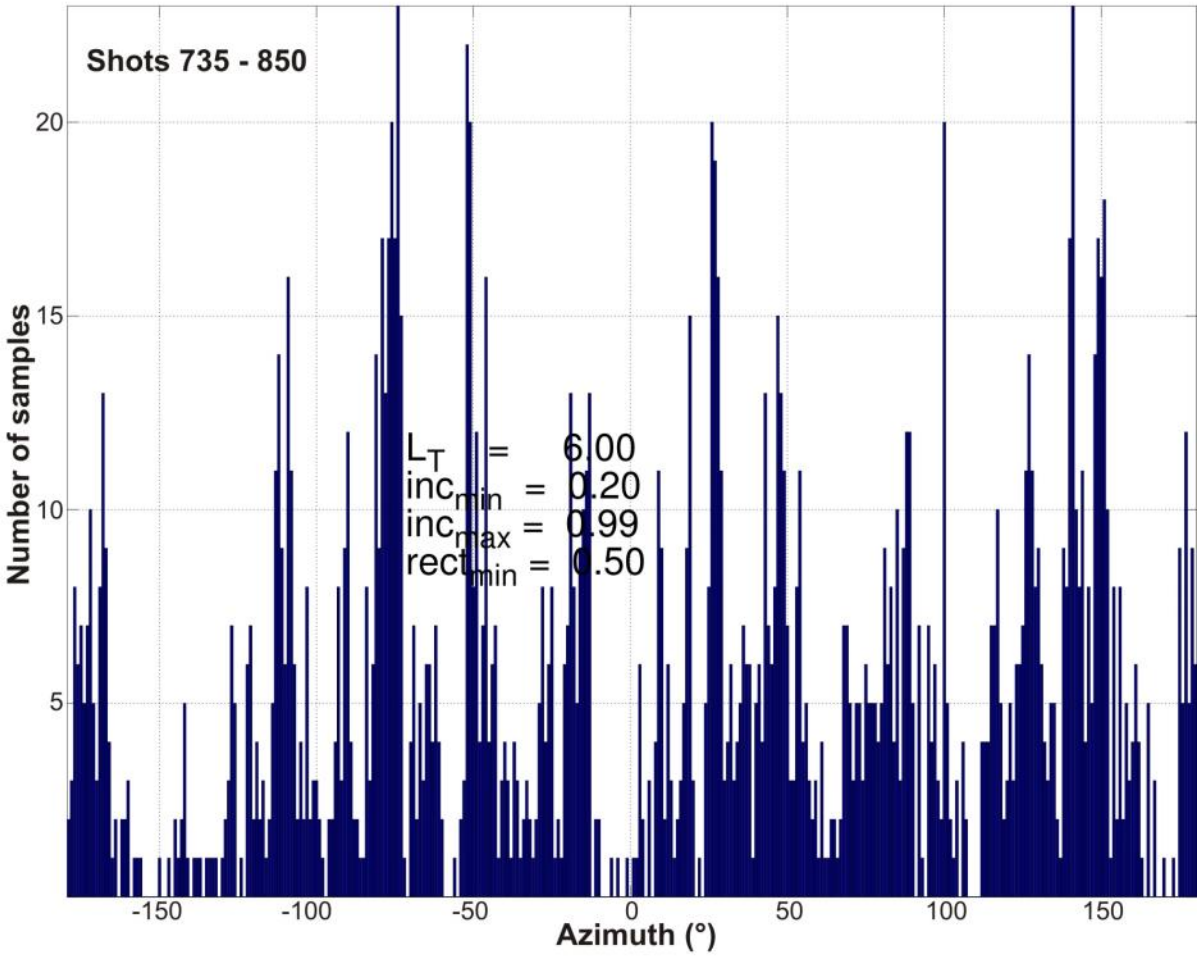

Figure 25. Results of the application of the Rosenberger (2010) azimuth-detection algorithm for station OBS-D, details see text.

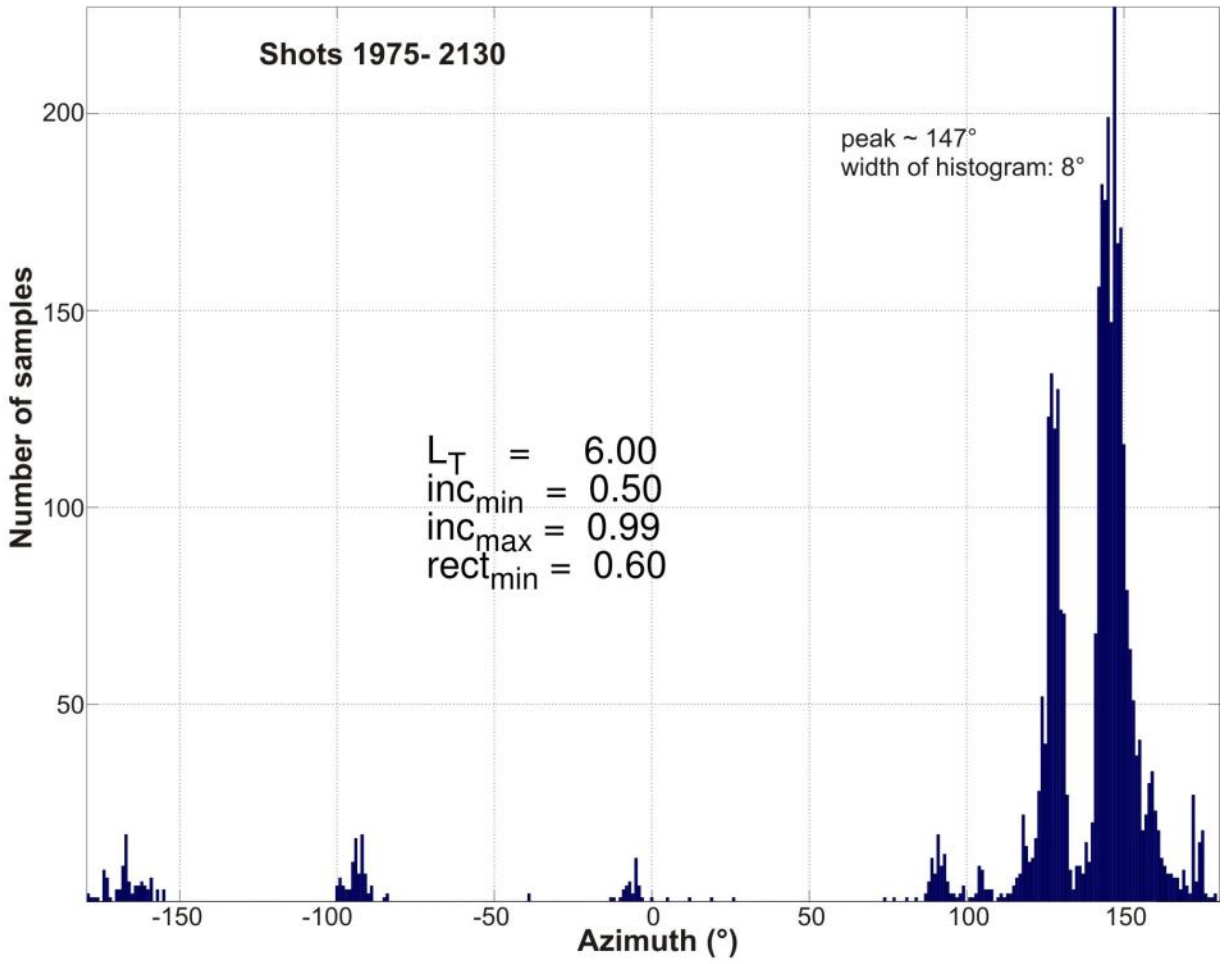

Figure 26. Results of the application of the Rosenberger (2010) azimuth-detection algorithm for station OBS-E (compare to map shown in Figure 17), details see text.

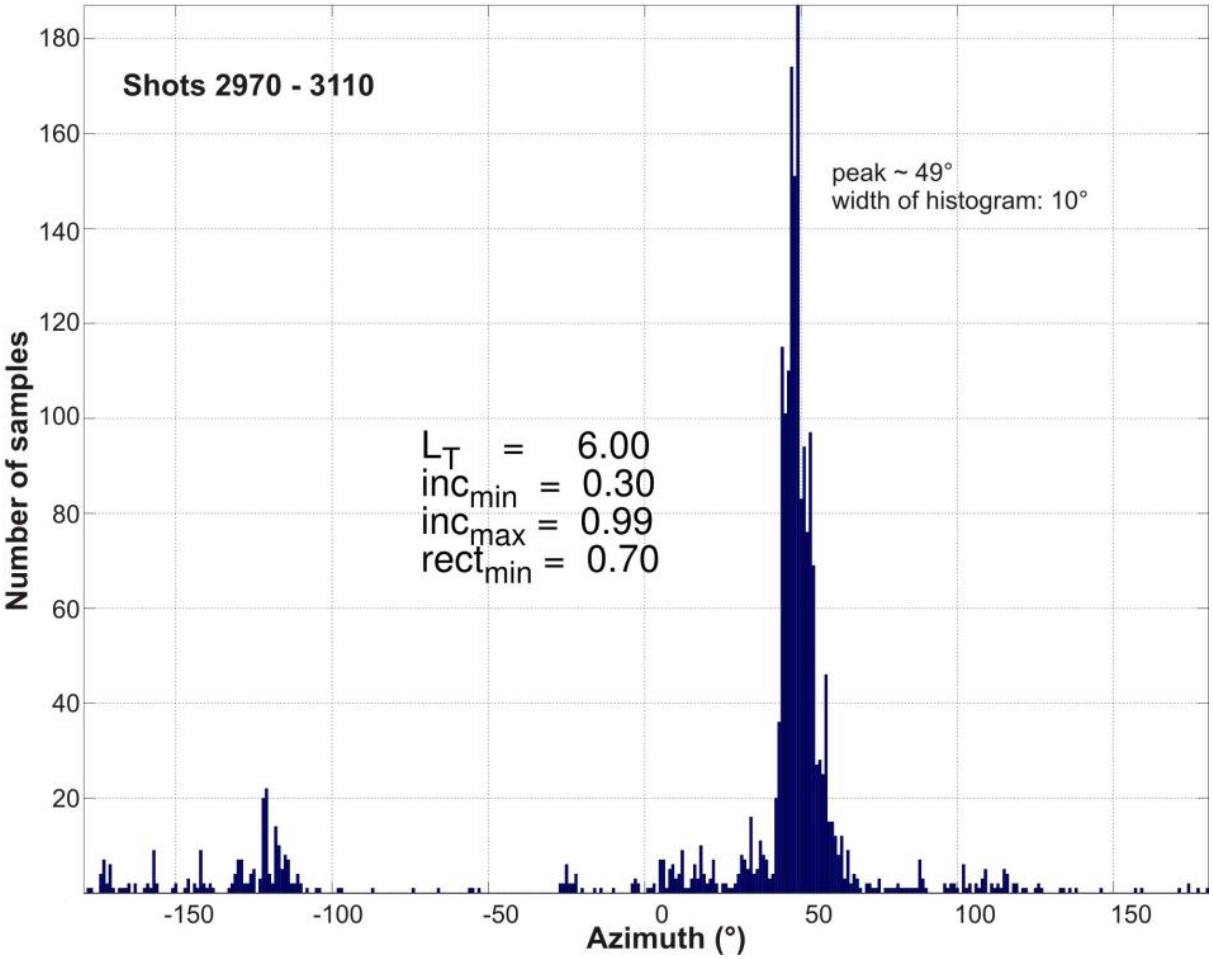

Figure 27a. Results of the application of the Rosenberger (2010) azimuth-detection algorithm for station OBS-F, shots 2970 – 3110, NE-SW trending shots across OBS station, compare to map shown in Figure 18, details see text.

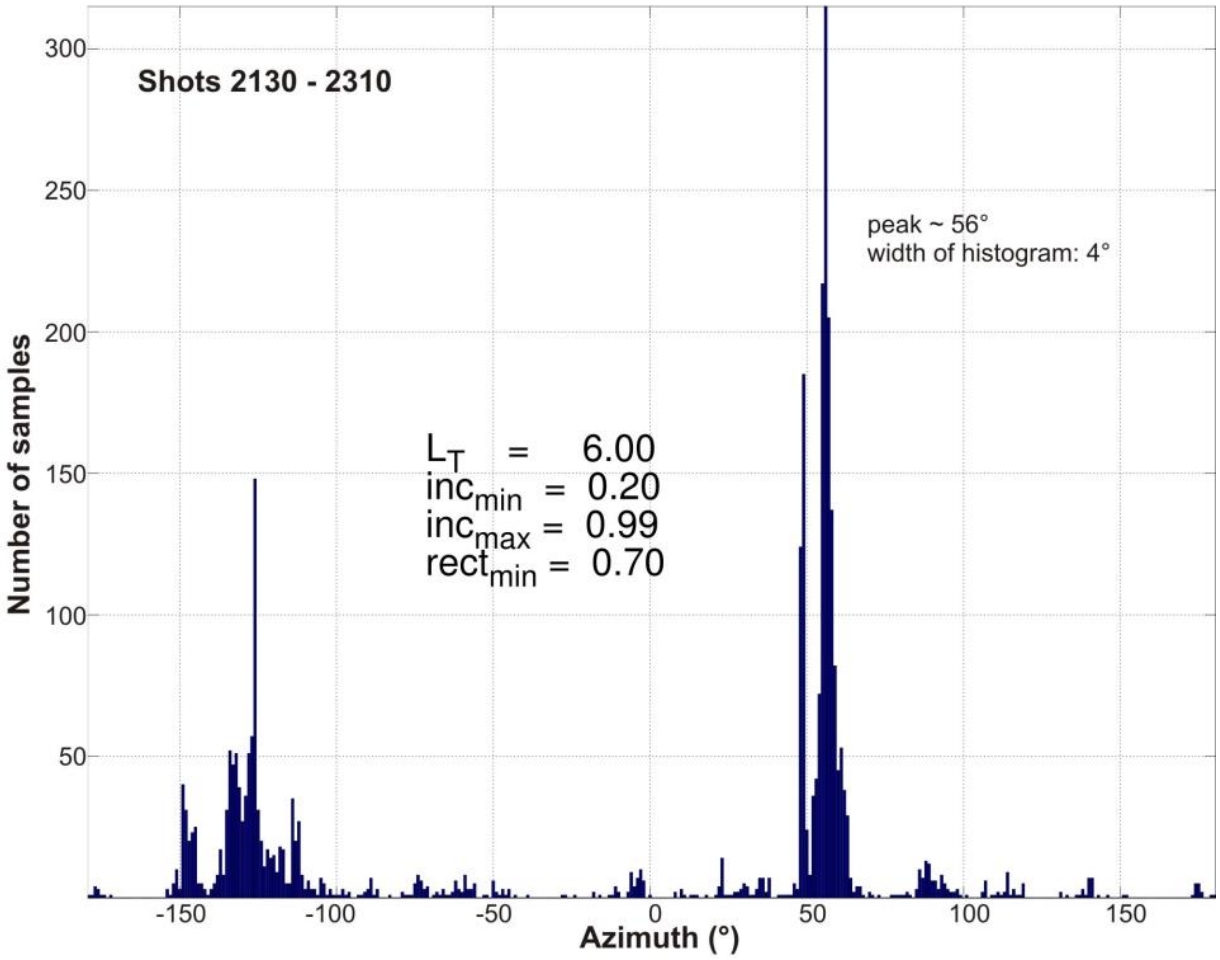

Figure 27b. Results of the application of the Rosenberger (2010) azimuth-detection algorithm for station OBS-F, shots 2130 – 2310, NW-SE trending shots across OBS station, compare to map shown in Figure 18; details see text.

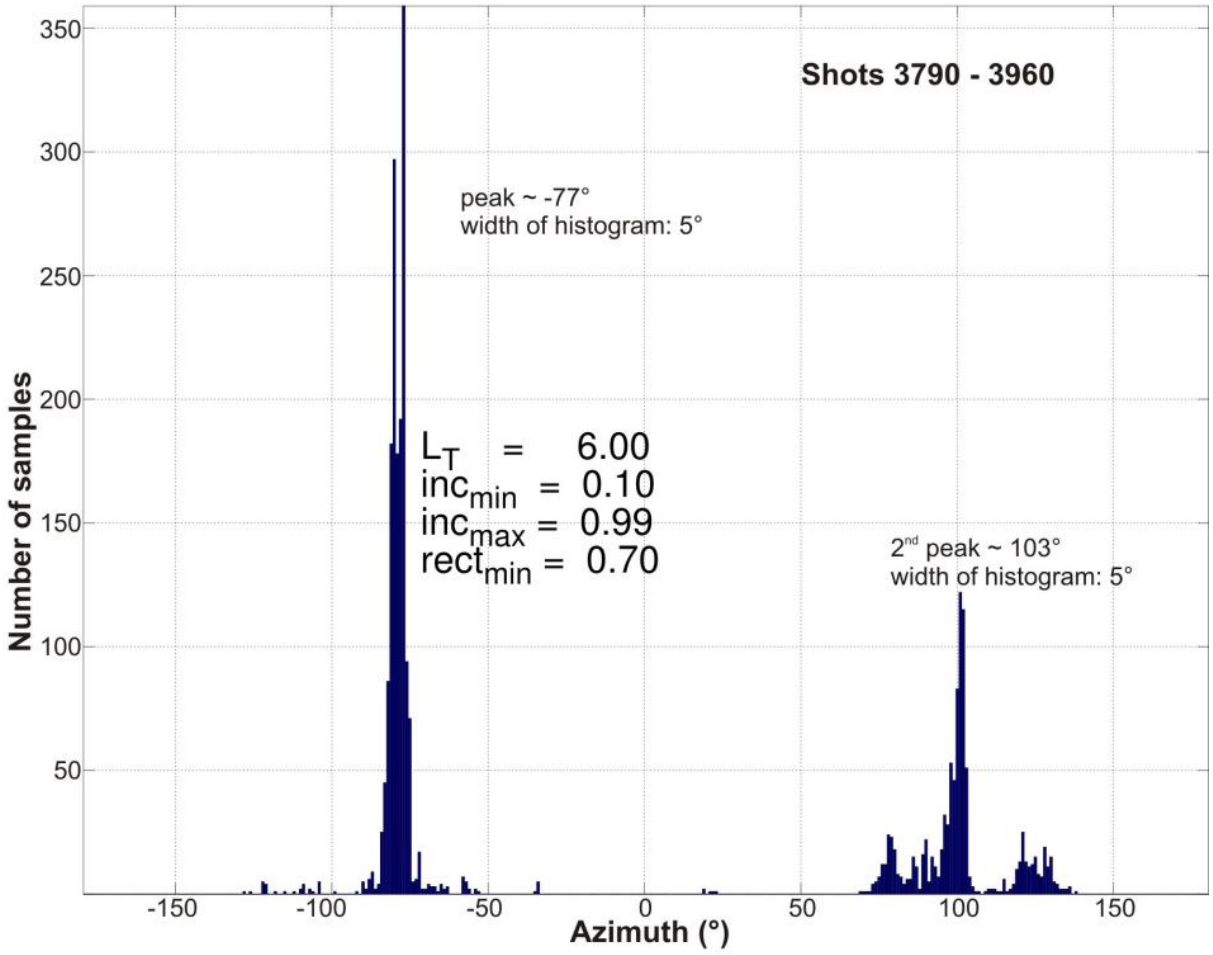

Figure 28a. Results of the application of the Rosenberger (2010) azimuth-detection algorithm for station OBS-H, crossing the station in NE-SW direction, compare to map shown in Figure 19; details see text. The 2nd peak represents the 180-degrees rotated possible solution, relative to the maximum peak.

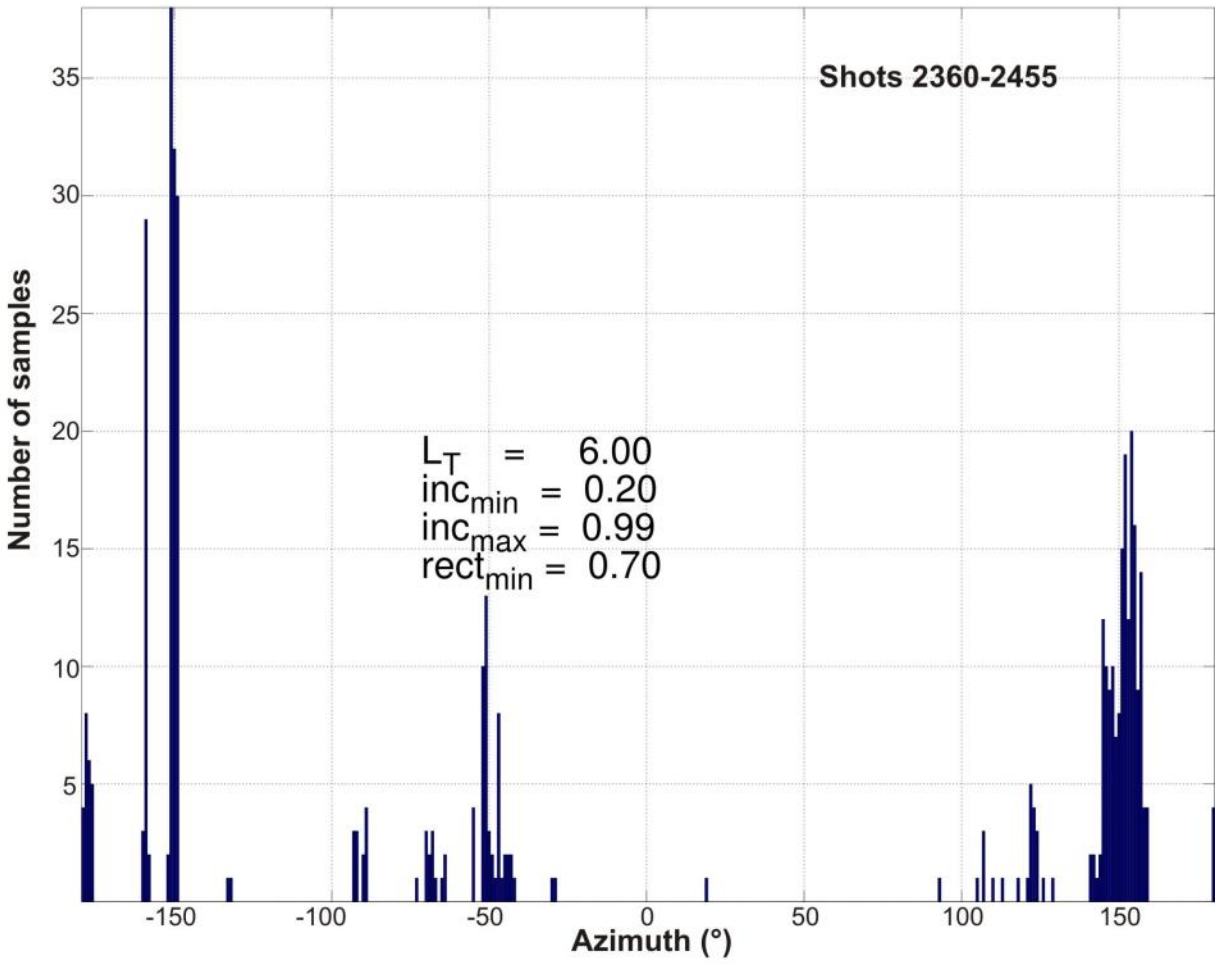

Figure 28b. Results of the application of the Rosenberger (2010) azimuth-detection algorithm for station OBS-H, crossing the station in NE-SW direction, compare to map shown in Figure 19; details see text. In this orientation, no conclusive solution can be found for the OBS azimuth, similar to the hodogram analysis shown in Figure 19.

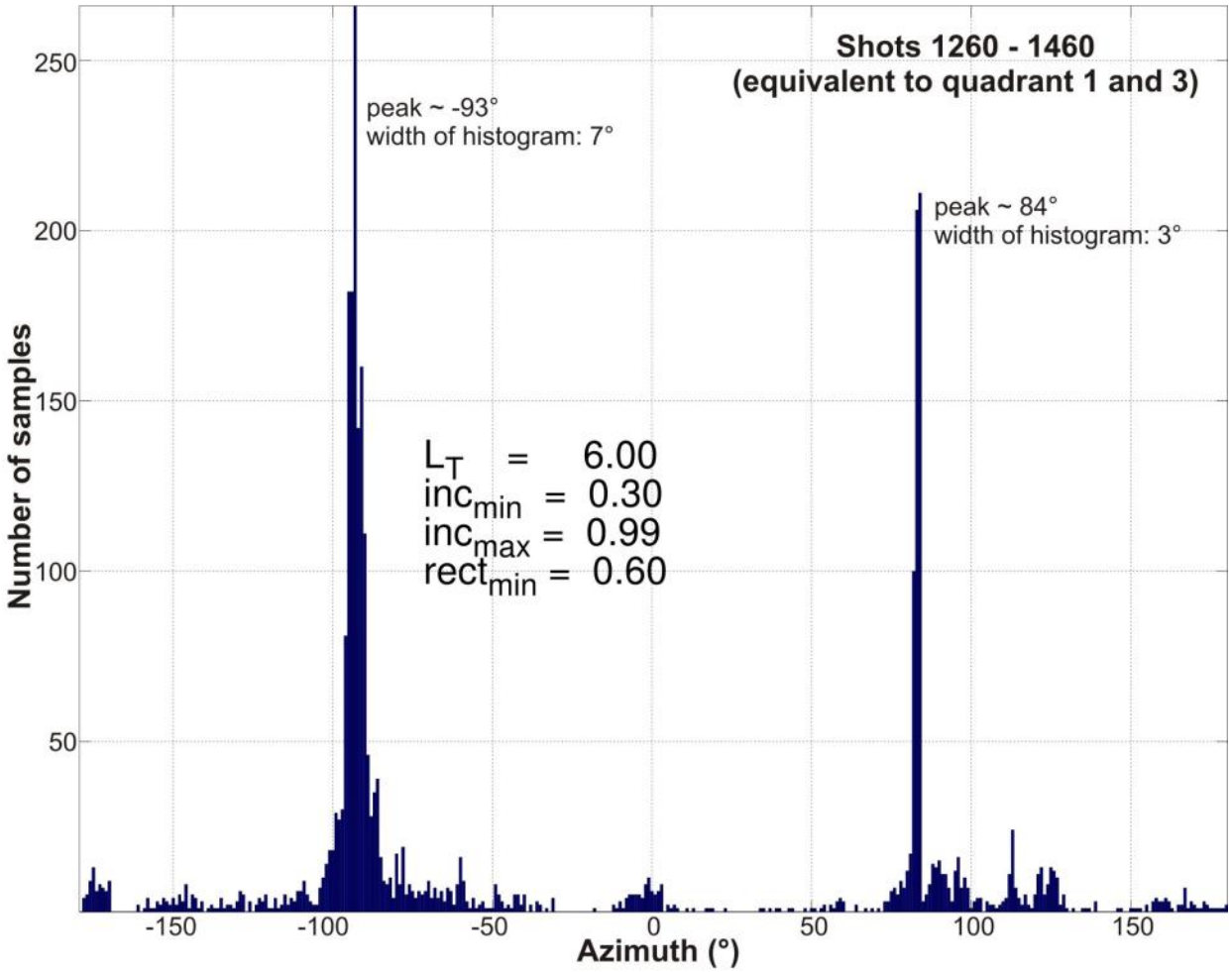

Figure 29a. Results of the application of the Rosenberger (2010) azimuth-detection algorithm for station OBS-J, compare to map shown in Figure 20, details see text. The 2nd peak (84°) represents the 180-degrees rotated possible solution, relative to the maximum peak (-93°).

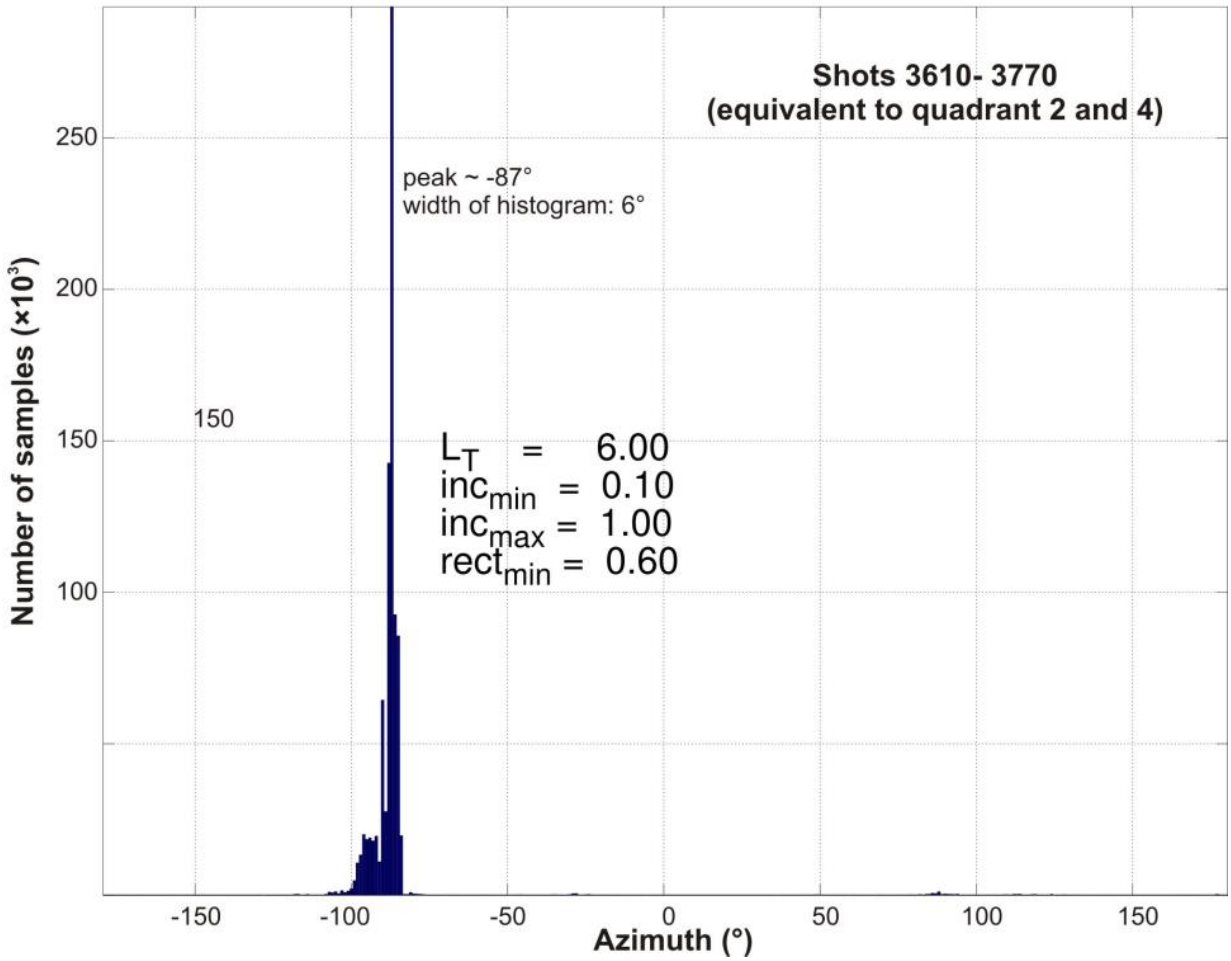

Figure 29b. Results of the application of the Rosenberger (2010) azimuth-detection algorithm for station OBS-J and shots from quadrants 2 and 4, compare to map shown in Figure 20, details see text.

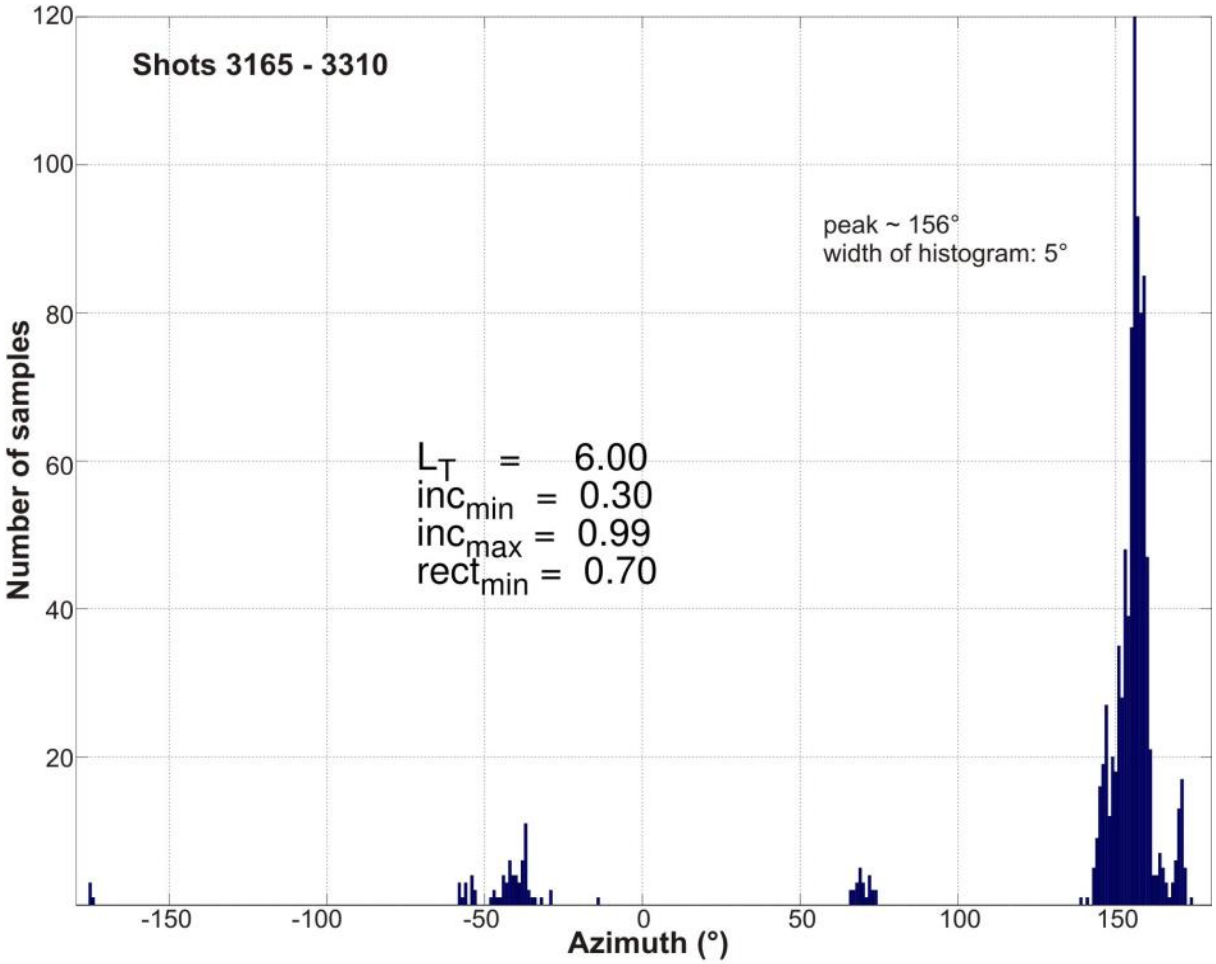

Figure 30a. Results of the application of the Rosenberger (2010) azimuth-detection algorithm for station OBS-K, shots 3165 – 3310, crossing the OBS station in a NE-SW orientation, compare to map shown in Figure 21, details see text.

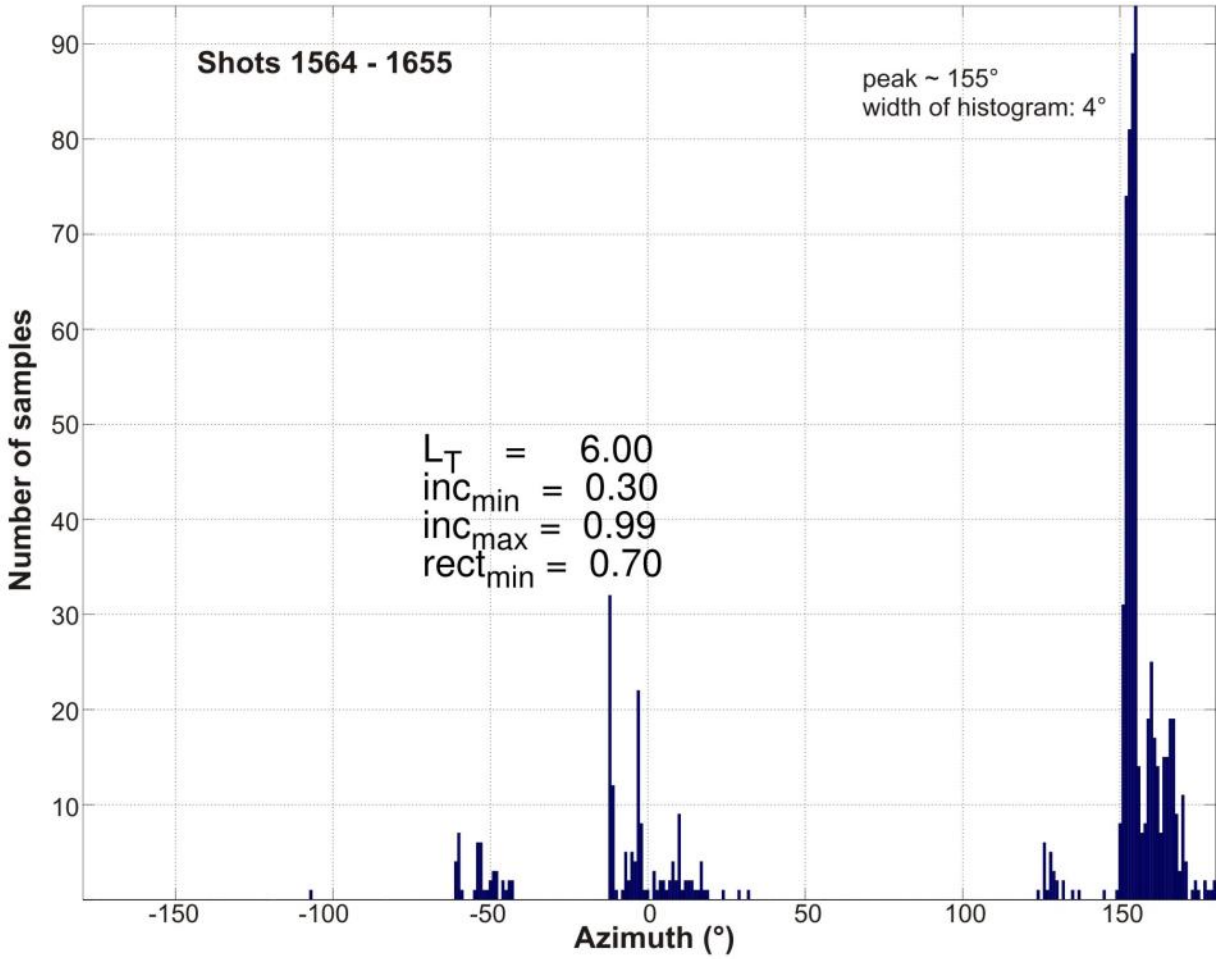

Figure 30b. Results of the application of the Rosenberger (2010) azimuth-detection algorithm for station OBS-K, shots 1564 – 1655, crossing the OBS station in a NW-SE orientation, compare to map shown in Figure 21; details see text.

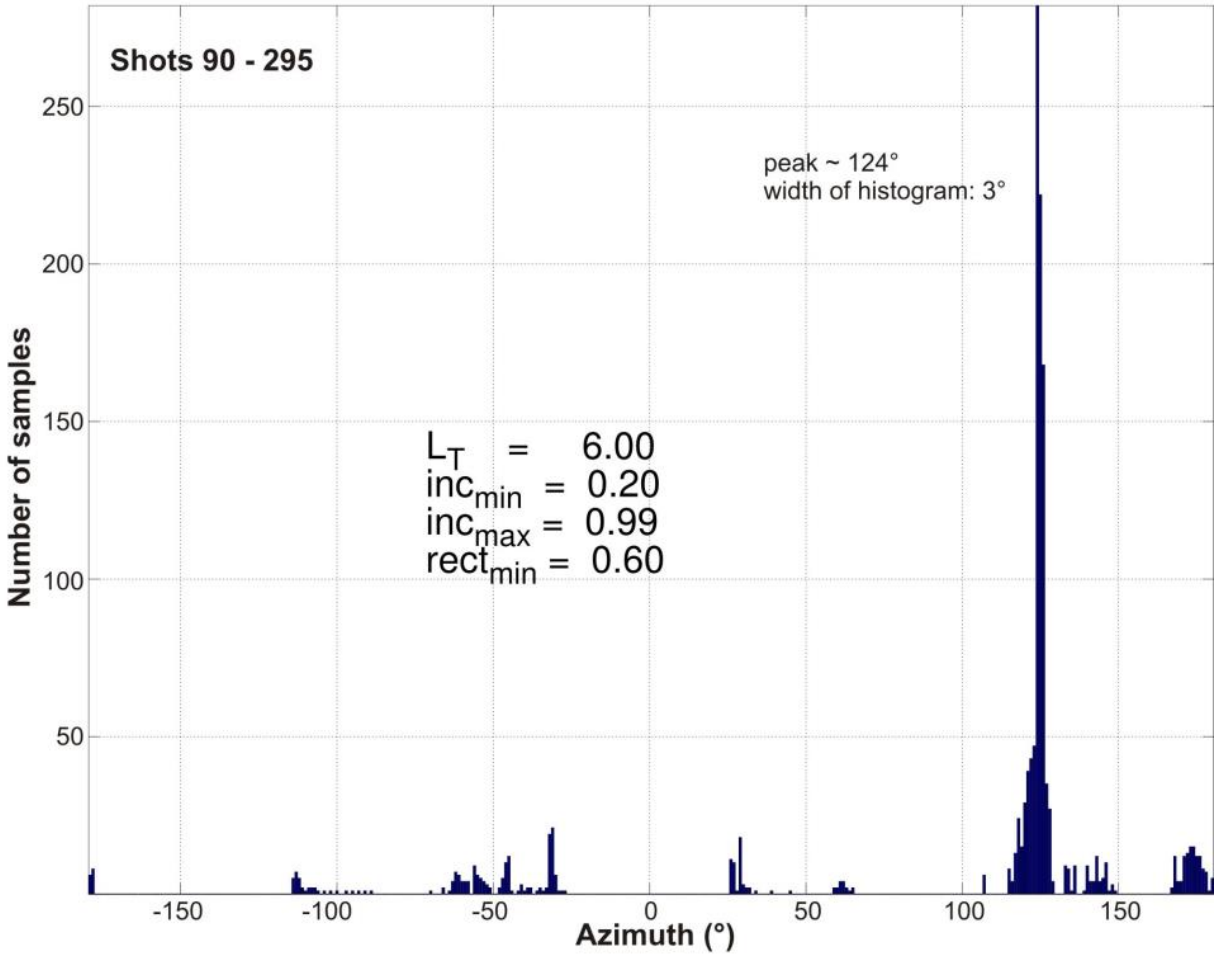

Figure 31. Results of the application of the Rosenberger (2010) azimuth-detection algorithm for station OBS-P, details see text.

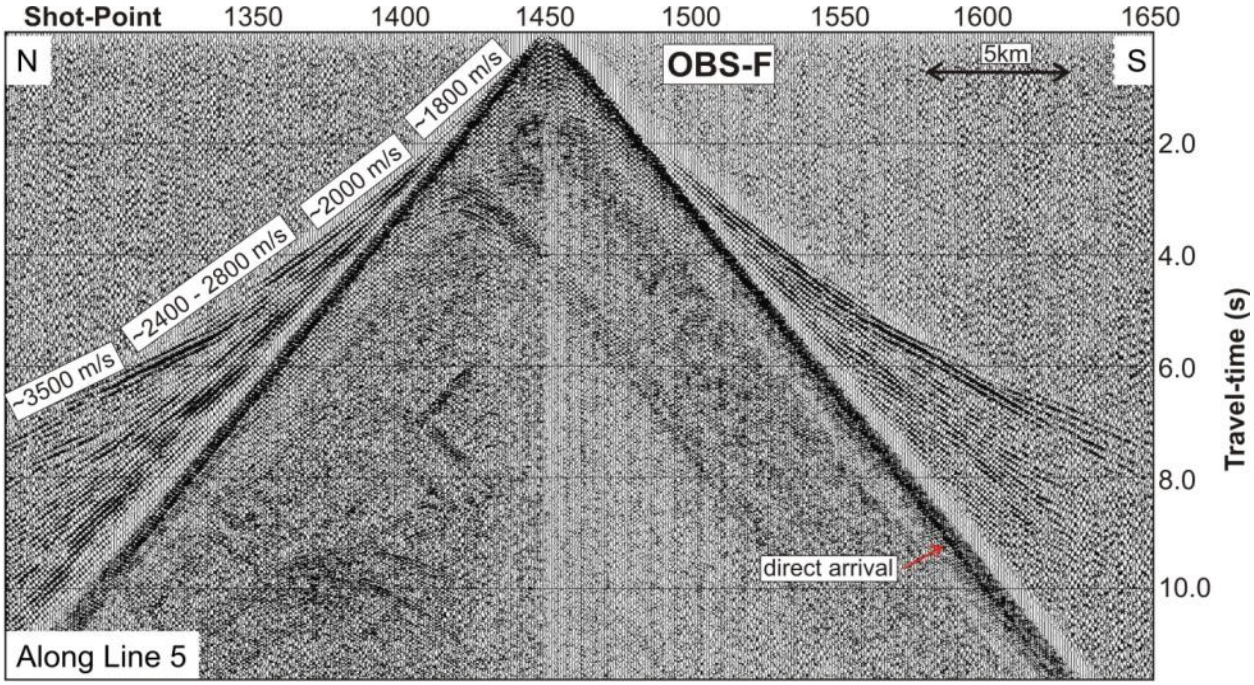

Figure 32. Example of the OBS data recorded on OBS-F (vertical component). Refractions are seen towards both sides of the seismic line acquired (Line-5, N-S oriented). Velocity values indicated are approximate, determined from linear-regression of the first arrivals identified.

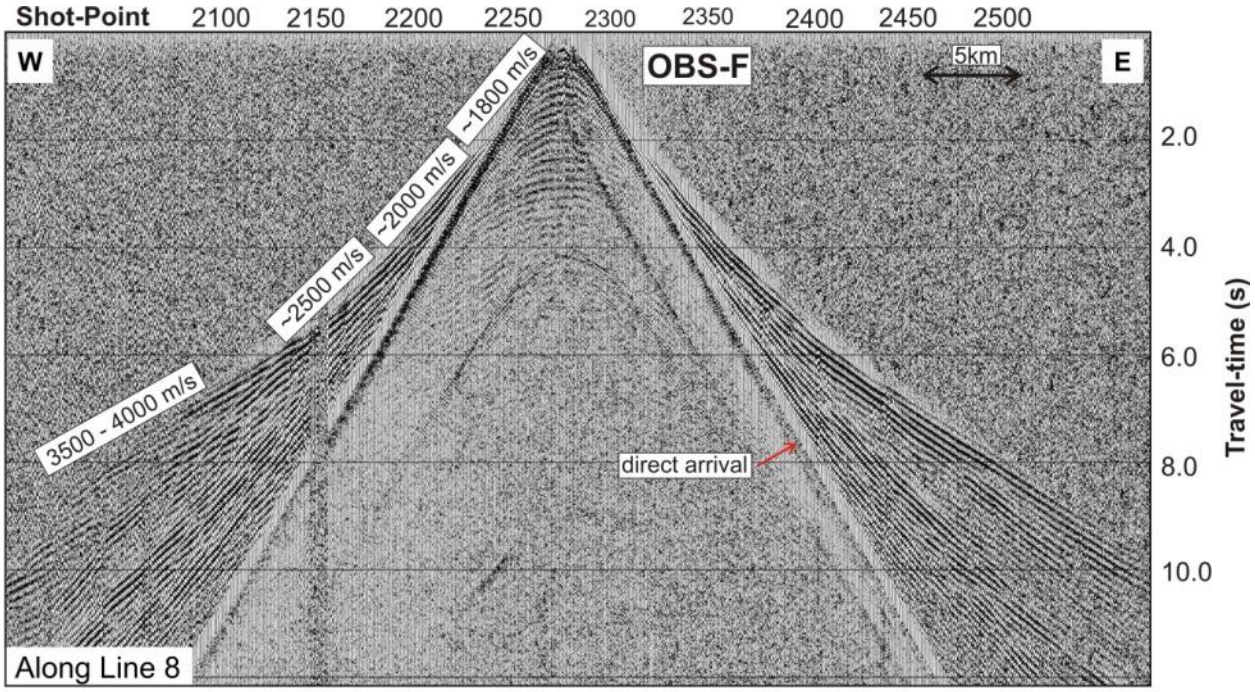

Figure 33. Example of the OBS data recorded on OBS-F (vertical component). Refractions are seen towards both side of the seismic line acquired (Line-8, E-W oriented). Velocity values indicated are approximate, determined from linear-regression of the first arrivals identified.

Appendix

Ocean Bottom Seismometer Deployment Logs

Shown are scans of the original handwritten field sheets for the OBS stations including information on battery levels pre- and post-deployment, and clock-drift parameters that were used to calculate drift-values as presented in Table 2.